Glycopeptidolipid glycosylation controls surface properties and pathogenicity in Mycobacterium abscessus

Wassim Daher, Louis-David Leclercq, Matt D. Johansen, Claire Hamela, Jona Karam, Xavier Trivelli, Jérôme Nigou, Yann Guerardel, Laurent Kremer

Glycopeptidolipid glycosylation controls surface properties and pathogenicity in *Mycobacterium abscessus*

Wassim Daher[1,5,&], Louis-David Leclercq[2,&], Matt D. Johansen[1,3], Jona Karam[1], Xavier Trivelli[6], Jérôme Nigou[4], Yann Guérardel[2,7,#], and Laurent Kremer[1,5,#,*]

[1]Centre National de la Recherche Scientifique UMR 9004, Institut de Recherche en Infectiologie de Montpellier (IRIM), Université de Montpellier, 1919 route de Mende, 34293, Montpellier, France.

[2]Univ. Lille, CNRS, UMR 8576 - UGSF - Unité de Glycobiologie Structurale et Fonctionnelle, F-59000 Lille, France.

[3]Centre for Inflammation, Centenary Institute and University of Technology Sydney, Faculty of Science, School of Life Sciences, Sydney, NSW, Australia.

[4]Institut de Pharmacologie et de Biologie Structurale, Université de Toulouse, CNRS, Université Paul Sabatier, Toulouse, France.

[5]INSERM, IRIM, 34293 Montpellier, France.

[6]Univ. Lille, CNRS, INRAE, Centrale Lille, Univ. Artois, FR 2638 - IMEC - Institut Michel-Eugène Chevreul, F-59000 Lille, France.

[7]Institute for Glyco-core Research (iGCORE), Gifu University, Gifu, Japan.

[#]For correspondence: E-mails yann.guerardel@univ-lille.fr, Tel: (+33) 3 20 33 63 47; laurent.kremer@irim.cnrs.fr, Tel: (+33) 4 34 35 94 47.

[*]Lead contact

[&]These authors contributed equally to this work.

HIGHLIGHTS

- Gtf1, Gtf2 and Gtf3 transfer deoxy-talose, the internal and extra rhamnose on GPL
- Gtf3 is required for efficient uptake of *M. abscessus via* the mannose receptor
- Deletion of Gtf1 or Gtf2 leads to rough corded bacilli and increased virulence
- GPL glycosylation controls *M. abscessus* surface properties and pathogenicity

SUMMARY

Mycobacterium abscessus is an emerging and difficult-to-manage mycobacterial species that exhibits smooth (S) or rough (R) morphotypes. Disruption of glycopeptidolipid (GPL) production results in transition from S to R and severe lung disease. A structure-activity relationship study was undertaken to decipher the role of GPL glycosylation in morphotype transition and pathogenesis. Deletion of *gtf3* uncovered the prominent role of the extra rhamnose in enhancing mannose receptor-mediated internalization of *M. abscessus* by macrophages. In contrast, the absence of the 6-deoxy-talose and the first rhamnose in mutants lacking *gtf1* and *gtf2*, respectively, only slightly affected *M. abscessus* phagocytosis but resulted in the S-to-R transition. Strikingly, *gtf1* and *gtf2* mutants displayed a strong propensity to form cords and abscesses in zebrafish, leading to robust and lethal infection. Together, these results underscore the importance and differential contribution of GPL monosaccharides in promoting virulence and infection outcomes.

KEYWORDS: *Mycobacterium abscessus*, morphotype, glycopeptidolipid, rhamnose, glycosyltransferase, macrophage, internalization, mannose receptor, zebrafish, virulence.

INTRODUCTION

Mycobacterium abscessus is a non-tuberculous mycobacteria (NTM), recognized as a multidrug-resistant species that has recently emerged as a major threat to individuals with underlying lung diseases such as chronic obstructive pulmonary disease (COPD) or cystic fibrosis (CF) (Floto et al., 2016; Johansen et al., 2020a). Infections with this fast-growing mycobacteria result in accelerated inflammatory lung damage (Esther et al., 2010), which may require surgical intervention (Ryan and Byrd, 2018). *M. abscessus* lung disease is difficult to treat due to intrinsic antimicrobial resistance, often leading to treatment failure despite prolonged multi-drug chemotherapy (Jarand et al., 2011; Johansen et al., 2020a; Kwak et al., 2019). Although originally thought to be acquired independently of the environment, the majority of individuals are infected with one of several dominant clones in circulation, indicating the presence of global transmission networks of *M. abscessus* and highlighting the possibility of human-to-human transmission (Bryant et al., 2016).

Distinguishable *in vitro* and *in vivo* properties have been assigned to smooth (S) or rough (R) variants of *M. abscessus* and include changes in sliding motility, biofilm formation, drug susceptibility (Bernut et al., 2016; Gutiérrez et al., 2018; Howard et al., 2006; Johansen et al., 2020b; Madani et al., 2019; Ryan and Byrd, 2018), bacterial surface hydrophobicity (Daher et al., 2020; Viljoen et al., 2018, 2020), aggregation, and cord formation (Bernut et al., 2014a, 2016; Howard et al., 2006; Viljoen et al., 2018). Other distinctive phenotypes influencing clinical disease outcome are related to intracellular interactions and trafficking in macrophages (Roux et al., 2016; Whang et al., 2017) or induction of potent pro-inflammatory responses (Roux et al., 2011). Numerous studies have highlighted the increased pathogenesis of the R variant as compared to the S variant (Bernut et al., 2014a, 2016, 2017; Catherinot et al., 2007). In this context, the zebrafish infection model has received considerable attention and represents a genetically tractable host-pathogen pairing for dissecting *M. abscessus* interactions with host immune cells (Bernut et al., 2015). Zebrafish are particularly susceptible to *M. abscessus* R infection, as evidenced by hyperinflammatory responses, increased bacterial burden, formation of massive serpentine cords and abscesses, resulting in enhanced larval mortality (Bernut et al., 2014a). These observations are consistent with epidemiological surveys, which showcase the prominence of the R variant in patients with severe lung infections and chronic airway colonization in CF patients (Catherinot et al., 2009; Jönsson et al., 2007). These findings underscore the clinical relevance of morphological distinctions between S and R morphotypes, and the need to identify the molecular mechanisms responsible for S-to- transition.

The transition from S to R relies on the production of high or low/absent levels of surface-associated glycopeptidolipids (GPL), respectively (Bernut et al., 2016; Gutiérrez et al., 2018; Howard et al., 2006; Medjahed et al., 2010). Genomic and transcriptomic studies have unraveled the presence of DNA insertions or deletions occurring in R forms, mainly in *mps1* and *mps2* encoding non-ribosomal peptide synthases responsible for the biosynthesis of the GPL peptide backbone, and *mmpL4a*/*mmpL4b* encoding membrane proteins involved in GPL transport (Bernut et al., 2016; Dedrick et al., 2021; Park et al., 2015; Pawlik et al.,

2013). Structurally, *M. abscessus* GPL comprises a peptide core consisting of an L-alaninol-linked D-phenylalanine-D-*allo*threonine-D-alanine tripeptide assembled by Mps1 and Mps2, which is acylated with a C_{24}-C_{33} 3-hydroxy/methoxy fatty acid. This lipopeptide is further decorated by a glycosylation arrangement that is built from *O*-methylated and *O*-acetylated deoxy hexoses (Daher et al., 2020; Ripoll et al., 2007; Whang et al., 2017). The lipopeptide is glycosylated with *allo*-Thr linked to a 6-deoxy-α-L-talose (6-dTal) while the terminal alaninol is linked to an α-L-rhamnose (Rha), producing the less-polar diglycosylated GPL species (GPL-2). In addition to GPL-2 that contain a 3,4-di-*O*-acetylated 6-dTal and a 3,4-di-*O*-methylated Rha, *M. abscessus* synthesizes more polar GPL species (GPL-3) *via* the addition of a 2,3,4-tri-hydroxylated Rha to the alaninol-linked 3,4-di-*O*-methylated Rha (Daher et al., 2020; Ripoll et al., 2007; Whang et al., 2017). GPL are heterogenous in structure and vary in length of the fatty acyl chain and the degree of hydroxylation or *O*-methylation of the glycosidic moieties through the action of *O*-methyltransferases, *O*-acetyltransferases and *O*-glycosyltransferases. However, the exact functions of these enzymes with respect to the GPL structure and their possible contribution to the pathogenicity of *M. abscessus* have not been addressed experimentally.

Many important interactions between bacterial pathogens and their host cells are highly specific receptor interactions that involve carbohydrates. Glycan interactions can mediate adhesion, invasion and immune evasion and be used by the pathogen to establish a successful infection (Poole et al., 2018). The question of whether GPL could take part in the adhesion and internalization of mycobacteria within cells has been proposed in previous studies. Pre-incubation of cells with blocking antibodies to complement receptor 3 (CR3) and mannose receptor (MR) partially abrogated the uptake of GPL-coated beads as well as phagocytosis of *Mycobacterium smegmatis* and *Mycobacterium avium*, which are GPL-producing NTM (Villeneuve et al., 2003, 2005). However, the structural elements of GPL that participate in recognition by CR3 and MR remain unknown. Furthermore, no information is available regarding the individual or collective contribution of the different GPL monosaccharides in the direct interaction with cell receptors during the early steps of interaction with host receptors, particularly within the context of *M. abscessus* pathogenesis.

Herein, we investigated the glyco-interactions of GPL with host cells by combining genetic, structural and biological studies. We performed a stepwise dissection of the three *gtf* genes that encode putative GPL glycosyltransferases in *M. abscessus.* This led to a panel of mutants that attempted to address the requirements and contribution of each monosaccharide in bacterial morphotypes, bacterial surface properties, adhesion and internalization of bacilli by human macrophages as well as pathogenicity in the zebrafish infection model. Synthesis of a GPL variant lacking 6-dTal and/or the first Rha in *gtf1* and *gtf2* mutants, respectively, was associated with an S-to-R morphotype transition showing hypercording and enhanced virulence and pathogenicity in zebrafish. We also provide evidence that the terminal Rha in GPL-3 enhances *M. abscessus* internalization by macrophages in a MR-dependent manner. Overall, this in-depth dissection of the GPL glycome provides new insights into the biological function and importance of the

different monosaccharides in the establishment of infection and disease pathology in this emerging human pathogen.

RESULTS

gtf1, *gtf2* and *gtf3* encode specific glycosyltransferases decorating GPL in *M. abscessus*.

The *gpl* locus encompasses three genes encoding putative glycosyltransferases, designated *gtf1-gtf3* **(Figure S1A)**. To investigate the contribution and biological functions of the corresponding glycosyltransferases in the GPL structure, *gtf1-gtf3* were deleted either individually or simultaneously in the GPL-producing S variant of *M. abscessus,* using a recently developed unmarked deletion system that allows for multiple gene deletion in *M. abscessus* (Richard et al., 2019) **(Figure S1A)**. PCR/sequencing performed on the parental and mutant strains using the primers in **Table S1** confirmed the proper genotype of the various *gtf* mutants **(Figure S1B)**. Genetic complementation of Δ1, Δ2 and Δ3 was done through specific integration at the *attB* chromosomal site (Stover et al., 1991) of a copy of *gtf1*, *gtf2* or *gtf3* with an HA tag at the 3'-end and placed under the control of the *hsp60* promoter (for *gtf1*) or their endogenous promoters (for *gtf2* and *gtf3*) **(Figure S1C)**. Probing the crude lysates from the various strains using anti-HA antibodies revealed a single band of the expected size, corresponding to Gtf1-HA, Gtf2-HA or Gtf3-HA proteins, validating complementation of the single mutants **(Figure S1D)**.

M. abscessus S synthesizes both diglycosylated (GPL-2a) and triglycosylated (GPL-3) GPL, containing one and two partially *O*-methylated Rha residues, respectively, in addition to the diacetyl-*O*-6-dTal residue **(Figure 1A)** (Daher et al., 2020). Thin layer chromatography (TLC) analysis of the polar fractions revealed a complex pattern of polar glycolipids, tentatively assigned to GPL-2a and GPL-3, all absent in *M. abscessus* R (Daher et al., 2020; Ripoll et al., 2007) **(Figure 1B)**. Monosaccharide compositional analysis confirmed the presence of the deoxyhexoses 6-dTal, Rha, and 3,4-di-*O*-methyl Rha in *M. abscessus* with a low proportion of 3-*O*-methyl Rha, suggesting the presence of minor isomers of GLP-2a and GPL-3, in which 3,4-di-*O*-methyl Rha is replaced by 3-*O*-methyl Rha **(Figure 1C)**. Mass spectrometry (MS) analysis showed two major signal patterns dominated by ion pairs at *m/z* 1258/1286 and 1404/1432, corresponding to GPL-2a and GPL-3, respectively (**Figure 1D**) (Daher et al., 2020). The presence of both acetyl groups on 6-dTal was confirmed by MS and MS/MS of polar glycolipids treated with mild alkali, resulting in a decrease of 84 m.u. at *m/z* 1174-1202 for GPL-2a and at *m/z* 1320-1348 for GPL-3 on the MS spectrum **(Figure S2A).** Comparison of the MS/MS fragmentation patterns of native and alkali-treated glycolipids confirmed the structure of GPL-3 and GPL-2a and the localization of acetyl groups on 6-dTal **(Figures 1E, 1F, S2B** and **S2C)**. Finally, MS analysis of individual bands (data not shown) confirmed the migration pattern of GPL on a TLC plate **(Figure 1B)**.

Deletion of *gtf3* leads to accumulation of GPL-2a whereas deletion of *gtf1* is associated with new GPL-1b and GPL-2b glycoforms.

TLC analysis showed that Δ3 accumulates a set of glycolipids, tentatively related to GPL-2a **(Figure 1B)**. MS analysis showed a pattern dominated by ion pairs at *m/z* 1258/1286 in the native fraction **(Figure 1D)** and *m/z* 1174-1202 on a saponified fraction **(Figure S2A)** that were identified as GPL-2a based on the MS/MS fragmentation pattern (data not shown). The absence of Rha in the polar glycolipid fraction confirmed that Δ3 fails to synthesize GPL-3 **(Figure 1C)**.

Δ1 and Δ1,3 synthesize a set of glycolipids different from the WT strain, characterized by the absence of GPL-2a and GPL-3 **(Figure 1B, 1C *and* 1D)**. MS analysis of Δ1 revealed two clusters of signals with a difference of 146 m.u centered at *m/z* 1188/1202 and 1014/1042 **(Figure 1D)**. MS/MS analysis of the characteristic parent ion at *m/z* 1188 established the presence of a terminal Rha-$(Me)_2$Rha-disaccharide through the observation of fragment ions M-146 at *m/z* 1042 and secondary ions at *m/z* 517/371 574/428 763/617 without loss of $(Ac)_2$dTal **(Figure S3A)**. MS/MS analysis of the characteristic parent ion at *m/z* 1042 established the presence of a terminal $(Me)_2$Rha residue owing to the observation of the fragment ion M-174 at *m/z* 867 and the absence of Rha and $(Ac)_2$dTal **(Figure S3B)**. MS analysis of saponified GPL did not show an 84 m.u. decrease, further demonstrating the absence of $(Ac)_2$dTal **(Figure S2A)**. Altogether, these analyses indicate that Δ1 synthesizes two new GPL isomers devoid of $(Ac)_2$dTal, designated GPL-2b and GPL-1b, substituted or not by a terminal Rha on the $(Me)_2$Rha. MS analysis of Δ1,3 showed a single cluster of signals with similar *m/z* values to GPL-1b **(Figure 1D)**. The MS/MS fragmentation pattern of the signal at *m/z* 1042 confirmed the identification of GPL-1b (**Figure S3C**). The presence of a single Rha was confirmed by homo- and heteronuclear NMR spectroscopy, as exemplified by the assignment of glycan and peptide moieties on the ^{1}H-^{13}C HSQC spectrum **(Figure S3D)**. In agreement with the compositional analysis (**Figure 1C**), two isomers of mono-glycosylated GPL-1b substituted with Rha or MeRha instead of $(Me)_2$Rha were also identified by MS/MS in the lipid polar fraction isolated from Δ1,3 (**data not shown** and **Figure 1C**).

Non-glycosylated lipopeptide intermediates accumulate in the *gtf2* mutant.

The absence of orcinol-sensitive bands on the TLC plate and the lack of GPL signal on the MS spectra implies that deletion of *gft2* abrogates GPL synthesis (**Figure 1B** and **1C**). However, staining with phospho-molybdic acid showed the accumulation of two compounds in Δ2 and Δ1,2, tentatively assigned to non-glycosylated GPL biosynthetic intermediates **(Figure S3E)**. The MALDI-TOF spectrum of the lower R_f polar lipid in Δ1,2 showed two intense ions at *m/z* 838 and 866 that can be attributed to the unmethoxylated C28 and C30 tripeptide bound to an alaninol residue **(Figures 1D** and **S3F)**. The ^{1}H-^{1}H COSY NMR spectrum confirmed the presence of three amino acids Ala, Thr and Phe as well as alaninol **(Figure S3G)**. Similar analyses of the polar

lipid with a higher R_f of Δ1,2 indicated the presence of the unmethoxylated C28 and C30 tripeptide linked to a valinol residue (data not shown).

Overall, structural analyses of the various *gtf* mutants identified at least 5 distinct GPL glycoforms **(Figure 2A)**. Similar to previous studies (Howard et al., 2006; Lee et al., 2017; Ripoll et al., 2007), we show here that GPL-3 and GPL-2a are predominantly synthesized in the WT S strain but absent in the R variant. While only GPL-2a is found in Δ3, the newly described GPL-1b and GPL-2b accumulated in Δ1. Δ2 and Δ1,2 do not produce GPL but accumulate non-glycosylated lipopeptide intermediates. Importantly, only GPL-1b was detected in Δ1,3 which implies that Gft1 could not transfer $(Ac)_2$dTal onto the unglycosylated lipopeptide and that the transfer of $(Me)_2$Rha by Gft2 precedes Gft1 activity, similar to *M. avium* (Eckstein et al., 2003) **(Figure 2B)**. In these two NTM species, Gtf2 in *M. abscessus* and its ortholog in *M. avium*, first catalyze the linkage between Rha and the branched-chain amino-alcohol, alaninol. Next, the addition of the second Rha to the first Rha or of 6-dTal to the threonine residue are accomplished by Gtf1 or Gtf3.

Deletion of *gtf1* or *gtf2* affects morphological and physiological properties of *M. abscessus in vitro*.

While it is well established that mutations in genes involved in peptide core production (*mps1* and *mps2*) or in transport (*mmpL4a* and *mmpl4b*) of GPL are responsible for the morphological S-to-R transition (Johansen et al., 2020a), the role of the different monosaccharides decorating the GPL backbone in this process remains unknown. We, therefore, appraised whether *gtf* deletions had an impact on colony morphology. Observations of individual colonies on Tryptic Soy agar show that, in contrast to the parental WT S progenitor, all mutants lacking either *gtf1* or *gtf2* (Δ1, Δ2, Δ1,2, Δ1,3, Δ2,3, and Δ1,2,3) formed rough, corded colonies **(Figure 3A)**. While functional complementation of Δ1 restored a smooth morphotype (Δ1_C), this was not the case for Δ2, despite apparent recovery of GPL production in Δ2_C **(Figure 3A)**. In contrast, deletion of *gtf3* did not affect the morphology of the strain, which remained smooth **(Figure 3A)**.

Partitioning of mycobacterial pellets between hexadecane and aqueous buffer has been used as a quantitative marker of cell surface hydrophobicity in mycobacteria to associate low pathogenicity with reduced hydrophobicity (Jankute et al., 2017). To determine whether the GPL glycan moieties affect the surface hydrophobicity, aqueous hexadecane-buffer partitioning was applied to the S, R, Δ1, Δ1_C, Δ2, Δ2_C, Δ3, Δ3_C, Δ1,2, Δ1,3, Δ2,3 and Δ1,2,3 strains. The Δ*fmt* mutant with a smooth phenotype, lacking the *O*-methyltransferase of the GPL lipid moiety, was included as a highly hydrophilic control strain (Daher et al., 2020). The complemented Δ*fmt* strain (Δ*fmt*_C) displaying parental hydrophobicity levels, was also added in this assay. Consistent with their colony morphotype, S, Δ3_C, and Δ*fmt*_C were more hydrophilic than the R, Δ1, Δ2, Δ1,2, Δ1,3, Δ2,3, and Δ1,2,3 strains, while Δ1_C and Δ2_C showed partial phenotype restoration **(Figure 3B)**. Only Δ3 and Δ*fmt* were significantly more hydrophilic than the parental S strain **(Figure 3B)**, suggesting that removal of 6-dTal and/or the internal Rha increases the surface hydrophobicity of *M.*

abscessus. This, however, does not affect the *in vitro* growth of the strains, indicating that deletion of the *gtf* genes does not impact the replication rate of *M. abscessus* in planktonic culture **(Figure S4A)**.

Previous studies demonstrated that smooth strains of *M. abscessus* display a higher capacity to slide on agar and a lower propensity to aggregate compared to rough strains (Deshayes et al., 2005; Martínez et al., 1999). We thus measured the sliding distances of the *gtf* mutants on 7H9 supplemented by 0.3% agar. All rough strains (except Δ2_C) showed significantly reduced motility compared to smooth strains **(Figure 3C)**. Consistently, all cord-forming mutants (rough strains) produced intense bacterial aggregates at the bottom of the glass tubes, while smooth strain cultures remained homogenous and turbid **(Figure S4B)**. This indicates that the *gtf1*- and *gtf2*-deletion mutants were associated with low sliding and high aggregation capacities. Whether this affects their ability to form biofilms was investigated using the Crystal Violet (CV) assay. The CV absorbance at 570_{nm} was ~2 fold higher for rough strains (except for Δ2_C) compared to smooth strains **(Figure 3D)**. In contrast, the CFU counts in the biomass formed at the bottom of the glass tubes were much higher in the smooth strains **(Figures 3E** and **S4D)**. Examination of biofilm formation in 6-well plates revealed that they were visible as pellicles at the air-liquid interface. The pellicles of the smooth variants appeared more filamentous and reticulated while those of rough variants appeared thinner **(Figure S4C)**.

We next investigated whether the glycan moieties affect the drug susceptibility profile of *M. abscessus* towards a panel of clinically used antibiotics. Although S and R strains shared comparable minimal inhibitory concentrations (MIC) to cefoxitin, imipenem, bedaquiline and amikacin, all R strains exhibited a 4-fold increase in susceptibility to rifabutin (MIC = 12.5 µg/mL) compared to S strains (MIC = 50 µg/mL) **(Figure S4E)**. These results highlight the importance of GPL glycosylation in resistance to rifabutin.

Deletion of *gft1* and *gtf2* leads to large extracellular cords and abscesses in zebrafish embryos.

The zebrafish embryo has recently emerged as an excellent model for studying the *in vivo* pathophysiology and drug susceptibility traits of NTM species, and in particular *M. abscessus* (Bernut et al., 2014b, 2014a; Johansen and Kremer, 2020). Embryos are optically transparent and display functional innate immunity from 24 hrs post-fertilization, allowing visualization of host-pathogen interactions in real-time using fluorescent bacterial reporters (Cronan and Tobin, 2014). Furthermore, exploitation of the zebrafish model uncovered the dissection of S and R variant virulence traits, with the R variant forming large serpentine bacterial cords that lead to abscess formation and tissue destruction, while the S variant leads to a chronic and comparatively avirulent disease phenotype (Bernut et al., 2014a). Thus, in this study, we sought to determine whether Δ1 and Δ2 maintain their rough phenotype in an *in vivo* setting, and whether they similarly display the pathophysiological signs of the R variant of *M. abscessus* infection. Infection of embryos with ~250-300 CFU of *M. abscessus* resulted in significant embryonic mortality in the WT R-infected, Δ1 or Δ2 groups compared to all other sets **(Figure 4A)**. Importantly, embryos infected with the complemented Δ1 or Δ2 strains, exhibited similar virulence to WT S strain. Furthermore, there was a significant increase in mortality in Δ2-

infected embryos compared with WT R, highlighting that this mutant displays greater virulence in the zebrafish embryo model. To further dissect the pathophysiological traits of *gtf* mutants compared to their WT counterpart, we examined the kinetics of extracellular cord and abscess formation in real-time using a fluorescent microscope. When examining extracellular cord formation, we observed that there was a significantly greater proportion of embryos with cords in wild-type R, Δ1 or Δ2 mutants compared with the parental WT S and corresponding complemented strains. This phenotype was apparent as early as 2 days post-infection (dpi), and was even more pronounced at 4 dpi **(Figure 4B)**. We observed significantly lower proportions of embryos with cords in the Δ1_C or Δ2_C complemented strains compared to their corresponding parental mutant, demonstrating that complementation abrogates cord formation in these mutants and further emphasizing that cord formation is a critical driver of increased virulence in these mutants. When we examined the total number of cords per embryo in each group, we identified a similar number of cords per embryo in the wild-type R, Δ1 or Δ2 groups, which differed significantly from the WT S and the complemented strains **(Figure 4C)**. Abscess formation is strongly correlated with cord formation, often arising due to unrestrained extracellular cord expansion leading to substantial tissue destruction at infection sites (Bernut et al., 2014a). As such, we further examined whether abscess formation differed in Δ1 or Δ2 compared with WT strains. We observed significantly increased abscess formation in the Δ2 group compared with the parental WT S and the complemented Δ2 groups as early as 2 dpi, highlighting a plausible mechanism for the increased virulence of this strain compared with the WT R **(Figure 4D** and **4F)**. At 4 and 6 dpi, we identified significantly greater proportions of embryos with abscesses in the wild-type R, Δ1 or Δ2 groups compared with the parental WT S and corresponding complemented strains. When we further stratified abscess formation in embryos, we identified that WT R, Δ1 or Δ2 groups displayed an increased number of abscesses per embryo compared with wild-type S and complemented strains. This confirms that abscess formation strongly correlates with the presence of extracellular cord formation in the zebrafish embryo **(Figure 4B-4F)**. Overall, using the zebrafish embryo, we can conclude that deletion of *gtf1* or *gtf2* leads to a stable rough phenotype that is preserved in an *in vivo* setting and displays the pathophysiological hallmarks of WT R infection, such as the large extracellular cord and abscess formation.

Strains lacking GPL production form cords that represent a typical marker and trait associated with acute infection and disease severity (Bernut et al., 2014c; Gutiérrez et al., 2018; Howard et al., 2006). The question remains whether smaller modifications, such as glycosylation, in the GPL structure induce cord formation, both within and outside the macrophage. To address this question, human THP-1 macrophages were individually infected with all strains of *M. abscessus* and the fate of the bacilli was examined at 3 dpi. Intracellular and extracellular giant cords were observed with all strains lacking either *gtf1* and/or *gtf2* **(Figure S5)**. Complementation of Δ1 inhibits cord formation in this strain, whereas complementation of Δ2 retains the ability to generate these bacterial structures **(Figure S5)**. These observations suggest a direct link between the absence of 6-dTal or the first Rha in cord formation.

6-dTal and di-Rha are required for *M. abscessus* uptake by macrophages.

Glycans displayed at the surface of microbial pathogens play an important role in mediating early interactions between microbes and the host, facilitating the first steps of infection. We investigated the impact of GPL glycosylation on the adhesion and invasion of *M. abscessus* by human THP-1 macrophages. Cells were infected with *M. abscessus* S, R, Δ1, Δ1_C, Δ2, Δ2_C, Δ3, Δ3_C, Δ1,2, Δ1,3, Δ2,3 or Δ1,2,3 expressing tdTomato for 3 hrs at a multiplicity of infection (MOI) of 2:1, prior to assessing phagocytosis and intracellular growth. After infection and treatment with 250 µg/mL amikacin to prevent extracellular bacterial growth, macrophages were lysed at 3, 24, and 72 hrs post-infection (hpi) and plated to determine intracellular bacterial burden. At day 0 (3 hpi), the invasion rate of single, double and triple mutants was reduced by ~ 0.5 log compared with the parental WT S, and this effect was rescued in all complemented strains (Δ1_C, Δ2_C and Δ3_C) **(Figure 5A)**. This decrease in bacterial burden was maintained at 24 and 72 hpi **(Figure 5A)**. In parallel, at 3, 24, and 72 hpi, macrophages were stained with anti-CD43 and DAPI. Microscopic observations and quantification of infected cells revealed a marked reduction in the number of THP-1 cells infected with single, double and triple mutants immediately after phagocytosis. This effect was also maintained over time compared with cells infected with WT progenitors or complemented strains **(Figure 5B** and **5C)**. To assess the consequences of the invasion defect on intracellular bacterial loads, infected macrophages were classified into three categories at 3 hpi based on their bacterial content: weakly infected (<5 bacilli), moderately infected (5−10 bacilli) and heavily infected (>10 bacilli), as illustrated in **Figure 5D**. This quantitative analysis indicates that deletion of the *gtf* genes in single, double and triple mutants profoundly reduced the percentage of moderately and heavily infected THP-1 cells while increasing the proportion of the weakly infected category **(Figure 5C** and **5D)**. Together, this indicates that i) GPL are involved in *M. abscessus* internalization by macrophages, and ii) deoxy-talose and extra rhamnose are both required for optimal internalization.

As a first step to characterize the putative receptor(s) involved in *M. abscessus* entry into macrophages, we performed binding competition experiments. Since GPL monosaccharides are involved in the uptake of *M. abscessus* by macrophages and *M. smegmatis* GPL have previously been reported to interact with the macrophage Mannose Receptor (MR) and the lectin domain of Complement Receptor 3 (CR3) (Villeneuve et al., 2005), we investigated the possible involvement of three lectins, MR, CR3, and Dectin-1, a β-glucan-binding lectin (Brown and Gordon, 2001) like CR3. Therefore, cells were pre-treated 1 hr prior to infection with 100 µg/mL of soluble ligands of each of the three lectins: mannan for MR (Shepherd et al., 1983), laminarin for Dectin-1 and CR3 (Gantner et al., 2005; Xia and Ross, 1999), or methyl-α-D-glucopyranoside for CR3 (Lin et al., 2010). At 3 hpi, intracellular bacterial loads were assessed by determination of CFU but no significant impact of the various pre-treatments was observed on the ability of the different strains, S, Δ1, Δ2, Δ3 or Δ1,3, to invade THP-1 cells under the conditions tested **(Figure S6)**. These competition assays do

not establish the participation of MR, CR3, and Dectin-1 in the internalization of *M. abscessus* S by macrophages. This could be due to the heterogenous composition of GPL, consisting of both diglycosylated (GPL-2) and triglycosylated (GPL-3) forms of GPL, which mitigates the potential involvement of GPL-3 in bacterial uptake (Daher et al., 2020).

Di-rhamnosylation of GPL enhances the uptake of *M. abscessus* by macrophages.

To assess the contribution of GPL-3 in *M. abscessus* uptake, we tipped the GPL-2/GPL-3 balance in favor of GPL-3. To do so, we cloned the *gtf3* gene in fusion with an HA tag in pMV261 (pMV261-*gtf3-HA*), which was used to generate the Gtf3_ov strain. Overproduction of Gtf3-HA was confirmed by Western blotting using anti-HA antibodies. In Gtf3_ov, the level of Gtf3 production was greatly increased compared with the level in Δ3_C carrying the integrative pMV306-*gtf3-HA*, unlike KasA **(Figure 6A)**. To test whether Gtf3 overexpression increased the proportion of the GPL-3/GPL-2 ratio, whole polar lipids were extracted and analyzed by TLC. The GPL profile of Gtf3_ov was shifted to bands migrating closer to the origin, as would be expected for the accumulation of GPL-3 subspecies with a concomitant reduction in GPL-2 subspecies **(Figure 6B)**. This indicates that in Gtf3_ov, most of the GPL-2 forms were converted to the corresponding GPL-3 forms, making this strain particularly useful for further investigate the role of the extra Rha in functional assays.

Gtf3_ov remained smooth **(Figure 3A),** grew similarly to the parental S strain in planktonic cultures **(Figure S4A)**, was more hydrophobic than the parental CIP104536^{T} (S) strain **(Figures 3B** and **S4B)** while exhibiting reduced sliding motility **(Figure 3C)** and produced high biomass of bacteria **(Figure 3E)**. Next, we interrogated whether increasing the GPL-3/GPL-2 ratio influences the early interactions between *M. abscessus* and macrophages. THP-1 macrophages were infected with either the parental S strain producing both GPL-2 and GPL-3 glycoforms or with Gtf3_ov producing mainly GPL-3. The uptake of Gtf3_ov was significantly increased (0.8 log at 3 hpi and >1 log at 24 and 72 hpi) compared with parental *M. abscessus* **(Figure 6C)**. Similar results were obtained using primary human monocyte-derived macrophages at 3 hpi **(Figure 6D)**. Moreover, the percentage of infected macrophages was increased 2-fold with Gtf3_ov compared to *M. abscessus* S **(Figure 6E** and **6F)**. Furthermore, the category of infected macrophages containing >10 bacilli increased significantly at 3, 24 and 72 hpi **(Figure 6E** and **6G)**. Importantly, internalization of Gtf3_ov by macrophages pre-treated with mannan, laminarin or methyl-α-D-glucopyranoside was inhibited by 35%, 45% and 50%, respectively **(Figure 6H)**, suggesting that MR, Dectin-1, and/or CR3 may be involved in the recognition of the recombinant strain and in the interaction with GPL-3. Collectively, these results suggest that early interactions of Gtf3_ov with and phagocytosis by macrophages are conditioned by the extent of GPL rhamnosylation and are dependent on the lectin receptor(s).

Enhanced phagocytosis of GPL-3-coupled beads is mediated by C-type lectin and β-glucan receptors.

The importance of GPL-3 in the early interaction of *M. abscessus* with host cells prompted us to conduct an in-depth analysis to evaluate the contribution of each GPL monosaccharide in phagocytosis. To eliminate interference from other bacterial surface molecules, four truncated forms of GPL produced in various *gtf* mutants were purified and coupled to green fluorescent beads (1 µm): GPL-1b substituted by a single Rha, GPL-2a substituted by 6-dTal and a single Rha, GPL-2b characterized by di-rhamnoside chain only and full GPL-3 comprising 6-dTal and di-Rhamnoside **(Figure 2A)**. Uncoated beads were included as negative control. The ability of the lipid-coated beads to enter macrophages was analyzed by pre-incubating THP-1 cells (~10 beads/cell) for 4 hrs, followed by immunofluorescence imaging. Quantification of the percentage of bead-containing cells clearly demonstrates that macrophages internalized significantly more GPL-2a-coaded beads (~ 2-fold), GPL-3-coaded beads (~ 5-fold) than GPL-1b- or GPL-2b-coaded beads **(Figure 7A** and **7B)**. Furthermore, THP-1 macrophages that phagocytosed GPL-3-coated beads contained an average of 4 beads/cell, whereas the average remains around 2 beads/cell for all other lipid-coated and uncoated beads **(Figure 7A** and **7C)**. High-resolution confocal 3D imaging confirmed the intracellular localization of the counted beads **(Figure S7A, Movies 1** and **2)**. Structure-function comparison of GPL-1b-, GPL-2a- and GPL-2b-conjugated beads indicates that the lack of 6-dTal or the extra Rha impairs the efficient uptake of GPL-coated beads **(Figure 7B)**, in agreement with results obtained with live bacteria.

Interestingly, uptake of GPL-2a- and GPL-3-beads was partially inhibited by mannan, laminarin or methyl-α-D glucopyranoside **(Figure 7D)**. Pre-incubation of cells with these compounds also significantly reduced the average number of GPL-3 beads/macrophage **(Figure S7B)**. To determine more specifically which lectin receptor(s) are involved in GPL binding, we performed antibody blocking experiments, using specific antibodies directed against MR, CR3 or Dectin-1. We found that phagocytosis of GPL2a- and GPL3-coupled beads was primarily dependent on MR **(Figures 7E, 7F** and **S7C)**. Phagocytosis of GPL3-coated beads was also dependent on CR3, although to a weaker extent **(Figure 7E** and **7F)**. No differences were observed for the uptake of GPL-1b or GPL-2b beads with any of the antibodies used **(Figure 7F)**. Quantitative measurements showed that the number of GPL-2a- or GPL-3-beads per macrophage is significantly reduced in the presence of MR and/or CR3 blocking antibodies **(Figure 7G)**. Overall, these results support a primarily role of MR in the recognition of GPL carbohydrates.

DISCUSSION

Most studies have reported the effects of near-total loss of GPL in *M. abscessus*, portraying an incomplete picture of the functions of these lipids in the pathogenesis of this emerging human pathogen while the structural elements related to these functions remain elusive. This study provides an in-depth overview of the structure-function relationship of GPL glycosylation and glyco-interactions with host receptors. We show

that in *M. abscessus*, Gtf1 transfers a 6-dTal to the threonine of the peptide core, while Gtf2 transfers Rha to alaninol and Gtf3 adds an extra Rha to the alaninol-bound Rha, similar to *M. smegmatis* (Miyamoto et al., 2006). Importantly, major and unexpected *in vitro* and *in vivo* phenotypes were uncovered using a set of genetically-defined *gft* mutants. Results indicate that GPL glycosylation 1) influences the hydrophilicity of the mycobacterial cell surface; 2) sustains the S morphotype; 3) facilitates the internalization of bacilli by macrophages; and 4) attenuates the virulence of *M. abscessus* in macrophages and in zebrafish embryos.

Low GPL production in *M. abscessus* results in a rough, hydrophobic strain, promoting bacterial aggregation and a reduced ability to form biofilms and slide (Daher et al., 2020; Viljoen et al., 2018). Lack of *O*-methylation of the GPL fatty acid chain, caused by *fmt* inactivation, increases the hydrophilicity of *M. abscessus* (Daher et al., 2020). Here, we demonstrate that loss of the 6-dTal or the internal Rha generates highly hydrophobic variants, with phenotypes similar to the WT R strain. Atomic force microscopy revealed that the surface of smooth bacilli comprises both hydrophilic and hydrophobic cell surface nanodomains (Viljoen et al., 2020). Therefore, it might be speculated that glycosylation of GPL present in hydrophilic nanodomains may mask important components required for the S-to-R transition, whereas specific loss of 6-dTal or total glycan moiety may expose these components, thereby affecting the cell surface composition and hydrophilic properties characterizing the S variant. Contrarily, the absence of terminal Rha residue does not affect drastically the hydrophilic balance, suggesting a tight regulation of the surface of bacilli. Thus, in addition to the chemical changes affected in the lipid portion of the GPL (Daher et al., 2020), these data point to an essential role of GPL glycosylation in bacterial surface properties.

Comparative studies between S and R variants highlighted the positive correlation between low GPL production and increased hydrophobicity with virulence in animal models (Gutiérrez et al., 2018; Johansen et al., 2020a). These features are indicative of the critical role that surface hydrophobicity has played in the evolution of *M. tuberculosis* toward greater pathogenicity and the assumption that increased hydrophobicity enhances aerosol transmission capacity and pathogenicity (Jankute et al., 2017). The fact that hydrophobic Δ1 and Δ2 mutants exhibit increased virulence in macrophages and in zebrafish supports this hypothesis. Strikingly, infection with both mutants was associated with large extracellular cord formation at comparable levels with the WT R, consistent with the fact that cording represents a hallmark of disease severity in this animal model (Bernut et al., 2014c). Due to their excessive size, *M. abscessus* cords cannot be ingested by professional phagocytes, leading to uncontrolled extracellular growth and abscess formation that rapidly leads to larval killing, as observed with Δ1 and Δ2. This clearly indicates that, in the presence of the sole innate immune system, the simple loss of 6-dTal and/or the internal Rha conveys a virulent phenotype and lethal infection in zebrafish embryos.

The outermost carbohydrate-rich bacterial layer represents the interaction interface between bacteria and host cells and is known to participate in adhesion and modulation of the immune response (Poole et al., 2018). L-Rha is an important component of mycobacterial cell walls (Mistou et al., 2016). Our results

emphasize the importance of GPL-associated Rha residues in controlling virulence and infectivity. L-Rha (6-deoxy-L-mannose) is a monosaccharide belonging to the deoxy-hexose family, commonly encountered in bacteria and plants (Wagstaff et al., 2021). Rha is ubiquitously incorporated into the surface carbohydrates of Gram-negative and Gram-positive bacteria (Wagstaff et al., 2021) and is a major constituent of the surface carbohydrates of pathogenic bacteria, such as *Shigella flexneri, Pseudomonas aeruginosa* or *Streptococcus pyogenes* (Wagstaff et al., 2021). In addition, previous work showed the crucial role of Rha-containing Lancefield antigens from group A *Streptococcus* and group B *Streptococcus* in bacterial growth and pathogenesis (Caliot et al., 2012). Therefore, in addition to their role in bacterial virulence and growth, our study indicates that di-Rha plays a direct role in the uptake of *M. abscessus* by macrophages. Since the internal Rha is mono- or di-methylated, additional studies are required to address whether methylation imparts on the internalization of *M. abscessus* by host cells. Similarly, *P. aeruginosa* mutants lacking the capacity to produce large D-Rha-rich polysaccharide antigens adhere less efficiently to human bronchial epithelial cells (Wagstaff et al., 2021). 6-dTal, which is the C2 epimer of 6-dGal, exerts important antimicrobial and anti-inflammatory properties, however data focused on the contribution to bacterial pathogenicity are scarce (Van Overtveldt et al., 2018). Our results incriminate 6-dTal, which is associated with attenuated virulence of *M. abscessus* in fish, as a determinant promoting bacterial cell entry. However, as 6-dTal is di-*O*-acetylated, it is unclear whether the phenotypes associated with $\Delta 1$ are directly related to the loss of the monosaccharide and/or caused by the absence of the two acetyl groups. The *M. abscessus gpl* locus possesses two genes, *atf1* and *atf2*, whose translation products transfer acetyl groups to 6-dTal sequentially (Ripoll et al., 2007). Future studies on *atf1* and *atf2* mutants are required to explore the potential involvement of GPL acetylation in *M. abscessus* morphotype, virulence and internalization by host cells.

Carbohydrates are known to interact with peptides through interactions involving hydrogen bonding with one or more hydroxyl acceptor groups of their constituting monosaccharide residues (Camiruaga et al., 2017; Roy et al., 2016). Considering GPL-3, the di-*O*-acetylated 6-dTal and the external Rha exhibit free hydroxyl groups (4 in total) that are likely to interact with their cognate receptors. In contrast, GPL-2a (lacking the extra Rha) possesses only 2 hydroxyl groups (one on the acetylated 6-dTal and one on the internal Rha), which may reduce hydrogen bonding and receptor affinity. Consistent with this hypothesis, phagocytosis assays indicate that GPL-2a and GPL-3 interact primarily with MR and to a lesser extent with CR3, and that receptor binding is augmented in the presence of the 6-dTal and the extra Rha in GPL-3. Accordingly, phagocytosis of the Gtf3_ov strain was inhibited by mannan. However, mannan pre-incubation had no impact on WT S uptake, most likely due to a heterogenous GPL composition comprising both GPL-2a and GPL-3 that may mask the contribution of di-rhamnosylated GPL in MR recognition. This suggests that other receptors are likely to be involved in the GPL-dependent uptake of *M. abscessus* S.

Rha, as indicated above, is structurally related to mannose and with its hydroxyl groups in equatorial positions at the *O*-3 and *O*-4 exhibits an optimal configuration for binding to the carbohydrate-recognition

domains of the mannose- and fucose-binding lectins, such as the MR (Feinberg et al., 2021; Zelensky and Gready, 2005). The mycobacterial envelopes are rich in mannose-containing glycoconjugates and several other ligands of the MR have been previously identified, such as the mannose-capped lipoarabinomannan (ManLAM) of *M. tuberculosis* or higher-order PIMs ($PIM_{5–6}$), which associate with the MR *via* their mannosylated α(1→2) motifs located at their non-reducing ends (Turner and Torrelles, 2018). The MR recognizes the terminal mannosyl unit of these motifs in Ca^{2+}-fashion *via* its carbohydrate-recognition domain 4, but supplementary interactions with the penultimate mannose residue allow an enhanced affinity for disaccharide motifs (Feinberg et al., 2021). In addition to MR, our data indicate binding of GPL3 to CR3, a heterodimer of α (CD11b) and β (CD18) transmembrane glycoproteins. It has been previously shown to recognize a mixture of di- and tri-glycosylated forms of *M. smegmatis* (Villeneuve et al., 2005). Its carbohydrate specificity is broader than initially appreciated, allowing it to react with a wide panel of polysaccharides containing mannose, glucose, as well as galactose (Poole et al., 2020; Thornton et al., 1996). CR3 has been involved in *M. tuberculosis* phagocytosis (Fenton et al., 2005) and mannosylated cell wall components, such as PIM_2, can bind directly to the lectin domain of CR3 (Villeneuve et al., 2005), arbitrating *M. tuberculosis* uptake by macrophages (Turner and Torrelles, 2018). Tal is structurally related to galactose. Although acetylated at positions 3 and 4 in GPL, the acetyl groups may allow hydrogen bonding to the receptors binding domain.

SIGNIFICANCE

Our results indicate that the monosaccharide composition of GPL from *M. abscessus* affects virulence and disease severity. It remains to be established whether GPL glycosylation is regulated in macrophages or during infection. Polar species of GPL in *M. smegmatis* are produced only under carbon starvation and induce smooth-colony formation (Mukherjee et al., 2005; Ojha et al., 2002), opening up the likelihood that the structure of GPL in *M. abscessus* is modulated in response to changing environments and during intracellular survival or infection. Thus, future studies should identify factors regulating the expression of *gtf1, gtf2* and *gtf3*, which would further enlighten our understanding of cell wall assembly and adaptation of *M. abscessus* to its host.

ACKNOWLEDGMENTS

This study was supported the French National Research Agency ANR-19-CE15-0012-01 (SUNLIVE). MDJ received a post-doctoral fellowship granted by Labex EpiGenMed, an «Investissements d'avenir» program (ANR-10-LABX-12-01). We acknowledge the Infectiopôle Sud Méditerranée for funding the PhD fellowship of JK. We are grateful to the Montpellier RIO Imaging facilities and the CRBM zebrafish facility (Montpellier), P. Richard and M. Plays for zebrafish husbandry, Fabien Blanchet for providing primary human macrophages. We are grateful to the PAGes core facility (http://plateforme- pages.univ-lille1.fr) and UMS 2014 - US 41 -

Plateformes Lilloises en Biologie & Santé for providing the scientific and technical environment conducive to achieving this work.

AUTHORS CONTRIBUTIONS

WD conceived and conducted experiments, analyzed the data, and wrote the manuscript. LDL, MDJ, JK and XT conducted experiments. LDL, MDJ, JN and YG analyzed the data and participated in writing the manuscript. LK conceived the idea of the project, analyzed the data and wrote the manuscript.

DECLARATION OF INTEREST

The authors declare no competing interests.

SUPPLEMENTAL INFORMATION

Supplemental Information includes 7 figures, 1 Table and 2 movies.

REFERENCES

Bernut, A., Herrmann, J.-L., Kissa, K., Dubremetz, J.-F., Gaillard, J.-L., Lutfalla, G., and Kremer, L. (2014a). *Mycobacterium abscessus* cording prevents phagocytosis and promotes abscess formation. Proc. Natl. Acad. Sci. U.S.A. *111*, E943-952.

Bernut, A., Le Moigne, V., Lesne, T., Lutfalla, G., Herrmann, J.-L., and Kremer, L. (2014b). *In vivo* assessment of drug efficacy against *Mycobacterium abscessus* using the embryonic zebrafish test system. Antimicrob. Agents Chemother. *58*, 4054–4063.

Bernut, A., Herrmann, J.-L., Kissa, K., Dubremetz, J.-F., Gaillard, J.-L., Lutfalla, G., and Kremer, L. (2014c). *Mycobacterium abscessus* cording prevents phagocytosis and promotes abscess formation. Proc. Natl. Acad. Sci. U.S.A. *111*, E943-952.

Bernut, A., Dupont, C., Sahuquet, A., Herrmann, J.-L., Lutfalla, G., and Kremer, L. (2015). Deciphering and imaging pathogenesis and cording of *Mycobacterium abscessus* in zebrafish embryos. J. Vis. Exp. *103*, e53130.

Bernut, A., Viljoen, A., Dupont, C., Sapriel, G., Blaise, M., Bouchier, C., Brosch, R., de Chastellier, C., Herrmann, J.-L., and Kremer, L. (2016). Insights into the smooth-to-rough transitioning in *Mycobacterium bolletii* unravels a functional Tyr residue conserved in all mycobacterial MmpL family members. Mol. Microbiol. *99*, 866–883.

Bernut, A., Herrmann, J.-L., Ordway, D., and Kremer, L. (2017). The diverse cellular and animal models to decipher the physiopathological traits of *Mycobacterium abscessus* infection. Front Cell Infect Microbiol *7*, 100.

Blanchet, F.P., Moris, A., Nikolic, D.S., Lehmann, M., Cardinaud, S., Stalder, R., Garcia, E., Dinkins, C., Leuba, F., Wu, L., et al. (2010). Human immunodeficiency virus-1 inhibition of immunoamphisomes in dendritic cells impairs early innate and adaptive immune responses. Immunity *32*, 654–669.

Brown, G.D., and Gordon, S. (2001). A new receptor for β-glucans. Nature *413*, 36–37.

Bryant, J.M., Grogono, D.M., Rodriguez-Rincon, D., Everall, I., Brown, K.P., Moreno, P., Verma, D., Hill, E., Drijkoningen, J., Gilligan, P., et al. (2016). Emergence and spread of a human-transmissible multidrug-resistant nontuberculous mycobacterium. Science *354*, 751–757.

Caliot, É., Dramsi, S., Chapot-Chartier, M.-P., Courtin, P., Kulakauskas, S., Péchoux, C., Trieu-Cuot, P., and Mistou, M.-Y. (2012). Role of the Group B antigen of *Streptococcus agalactiae*: a peptidoglycan-anchored polysaccharide involved in cell wall biogenesis. PLoS Pathog *8*, e1002756.

Camiruaga, A., Usabiaga, I., Insausti, A., León, I., and Fernández, J.A. (2017). Sugar–peptidic bond interactions: spectroscopic characterization of a model system. Phys. Chem. Chem. Phys. *19*, 12013–12021.

Catherinot, E., Clarissou, J., Etienne, G., Ripoll, F., Emile, J.-F., Daffé, M., Perronne, C., Soudais, C., Gaillard, J.-L., and Rottman, M. (2007). Hypervirulence of a rough variant of the *Mycobacterium abscessus* type strain. Infect. Immun. *75*, 1055–1058.

Catherinot, E., Roux, A.-L., Macheras, E., Hubert, D., Matmar, M., Dannhoffer, L., Chinet, T., Morand, P., Poyart, C., Heym, B., et al. (2009). Acute respiratory failure involving an R variant of *Mycobacterium abscessus*. J. Clin. Microbiol. *47*, 271–274.

Cronan, M.R., and Tobin, D.M. (2014). Fit for consumption: zebrafish as a model for tuberculosis. Dis Model Mech *7*, 777–784.

Daher, W., Leclercq, L.-D., Viljoen, A., Karam, J., Dufrêne, Y.F., Guérardel, Y., and Kremer, L. (2020). O-Methylation of the Glycopeptidolipid Acyl Chain Defines Surface Hydrophobicity of *Mycobacterium abscessus* and Macrophage Invasion. ACS Infect Dis *6*, 2756–2770.

Dedrick, R.M., Smith, B.E., Garlena, R.A., Russell, D.A., Aull, H.G., Mahalingam, V., Divens, A.M., Guerrero-Bustamante, C.A., Zack, K.M., Abad, L., et al. (2021). *Mycobacterium abscessus* Strain Morphotype Determines Phage Susceptibility, the Repertoire of Therapeutically Useful Phages, and Phage Resistance. MBio *12*.

Deshayes, C., Laval, F., Montrozier, H., Daffé, M., Etienne, G., and Reyrat, J.-M. (2005). A glycosyltransferase involved in biosynthesis of triglycosylated glycopeptidolipids in *Mycobacterium smegmatis*: impact on surface properties. J Bacteriol *187*, 7283–7291.

Eckstein, T.M., Belisle, J.T., and Inamine, J.M. (2003). Proposed pathway for the biosynthesis of serovar-specific glycopeptidolipids in *Mycobacterium avium* serovar 2. Microbiology (Reading) *149*, 2797–2807.

Esther, C.R., Esserman, D.A., Gilligan, P., Kerr, A., and Noone, P.G. (2010). Chronic *Mycobacterium abscessus* infection and lung function decline in cystic fibrosis. J. Cyst. Fibros. *9*, 117–123.

Feinberg, H., Jégouzo, S.A.F., Lasanajak, Y., Smith, D.F., Drickamer, K., Weis, W.I., and Taylor, M.E. (2021). Structural analysis of carbohydrate binding by the macrophage mannose receptor CD206. J Biol Chem 100368.

Fenton, M.J., Riley, L.W., and Schlesinger, L.S. (2005). Receptor-Mediated Recognition of *Mycobacterium tuberculosis* by Host Cells. Tuberculosis and the Tubercle Bacillus 405–426.

Floto, R.A., Olivier, K.N., Saiman, L., Daley, C.L., Herrmann, J.-L., Nick, J.A., Noone, P.G., Bilton, D., Corris, P., Gibson, R.L., et al. (2016). US Cystic Fibrosis Foundation and European Cystic Fibrosis Society consensus recommendations for the management of non-tuberculous mycobacteria in individuals with cystic fibrosis: executive summary. Thorax *71*, 88–90.

Gantner, B.N., Simmons, R.M., and Underhill, D.M. (2005). Dectin-1 mediates macrophage recognition of *Candida albicans* yeast but not filaments. EMBO J *24*, 1277–1286.

Gutiérrez, A.V., Viljoen, A., Ghigo, E., Herrmann, J.-L., and Kremer, L. (2018). Glycopeptidolipids, a Double-Edged Sword of the *Mycobacterium abscessus* Complex. Front Microbiol *9*, 1145.

Howard, S.T., Rhoades, E., Recht, J., Pang, X., Alsup, A., Kolter, R., Lyons, C.R., and Byrd, T.F. (2006). Spontaneous reversion of *Mycobacterium abscessus* from a smooth to a rough morphotype is associated with reduced expression of glycopeptidolipid and reacquisition of an invasive phenotype. Microbiology (Reading, Engl.) *152*, 1581–1590.

Jankute, M., Nataraj, V., Lee, O.Y.-C., Wu, H.H.T., Ridell, M., Garton, N.J., Barer, M.R., Minnikin, D.E., Bhatt, A., and Besra, G.S. (2017). The role of hydrophobicity in tuberculosis evolution and pathogenicity. Sci Rep *7*, 1315.

Jarand, J., Levin, A., Zhang, L., Huitt, G., Mitchell, J.D., and Daley, C.L. (2011). Clinical and microbiologic outcomes in patients receiving treatment for *Mycobacterium abscessus* pulmonary disease. Clin. Infect. Dis. *52*, 565–571.

Johansen, M.D., and Kremer, L. (2020). Large Extracellular Cord Formation in a Zebrafish Model of *Mycobacterium kansasii* Infection. The Journal of Infectious Diseases *222*, 1046–1050.

Johansen, M.D., Herrmann, J.-L., and Kremer, L. (2020a). Non-tuberculous mycobacteria and the rise of *Mycobacterium abscessus*. Nat Rev Microbiol *18*, 392–407.

Johansen, M.D., Daher, W., Roquet-Banères, F., Raynaud, C., Alcaraz, M., Maurer, F.P., and Kremer, L. (2020b). Rifabutin Is Bactericidal against Intracellular and Extracellular Forms of *Mycobacterium abscessus*. Antimicrob Agents Chemother *64*, e00363-20, /aac/64/11/AAC.00363-20.atom.

Jönsson, B.E., Gilljam, M., Lindblad, A., Ridell, M., Wold, A.E., and Welinder-Olsson, C. (2007). Molecular epidemiology of *Mycobacterium abscessus*, with focus on cystic fibrosis. J. Clin. Microbiol. *45*, 1497–1504.

Kwak, N., Dalcolmo, M.P., Daley, C.L., Eather, G., Gayoso, R., Hasegawa, N., Jhun, B.W., Koh, W.-J., Namkoong, H., Park, J., et al. (2019). *Mycobacterium abscessus* pulmonary disease: individual patient data meta-analysis. Eur. Respir. J. *54*.

Lamason, R.L., Mohideen, M.-A.P.K., Mest, J.R., Wong, A.C., Norton, H.L., Aros, M.C., Jurynec, M.J., Mao, X., Humphreville, V.R., Humbert, J.E., et al. (2005). SLC24A5, a putative cation exchanger, affects pigmentation in zebrafish and humans. Science *310*, 1782–1786.

Lee, S.-Y., Kim, H.-Y., Kim, B.-J., Kim, H., Seok, S.-H., Kim, B.-J., and Kook, Y.-H. (2017). Effect of amikacin on cell wall glycopeptidolipid synthesis in *Mycobacterium abscessus*. J. Microbiol. *55*, 640–647.

Lin, J.-S., Huang, J.-H., Hung, L.-Y., Wu, S.-Y., and Wu-Hsieh, B.A. (2010). Distinct roles of complement receptor 3, Dectin-1, and sialic acids in murine macrophage interaction with Histoplasma yeast. Journal of Leukocyte Biology *88*, 95–106.

Madani, A., Ridenour, J.N., Martin, B.P., Paudel, R.R., Abdul Basir, A., Le Moigne, V., Herrmann, J.-L., Audebert, S., Camoin, L., Kremer, L., et al. (2019). Cyclipostins and Cyclophostin Analogues as Multitarget Inhibitors That Impair Growth of *Mycobacterium abscessus*. ACS Infect Dis *5*, 1597–1608.

Martínez, A., Torello, S., and Kolter, R. (1999). Sliding motility in mycobacteria. J Bacteriol *181*, 7331–7338.

Medjahed, H., Gaillard, J.-L., and Reyrat, J.-M. (2010). *Mycobacterium abscessus*: a new player in the mycobacterial field. Trends Microbiol. *18*, 117–123.

Mistou, M.-Y., Sutcliffe, I.C., and van Sorge, N.M. (2016). Bacterial glycobiology: rhamnose-containing cell wall polysaccharides in Gram-positive bacteria. FEMS Microbiol Rev *40*, 464–479.

Miyamoto, Y., Mukai, T., Nakata, N., Maeda, Y., Kai, M., Naka, T., Yano, I., and Makino, M. (2006). Identification and characterization of the genes involved in glycosylation pathways of mycobacterial glycopeptidolipid biosynthesis. J. Bacteriol. *188*, 86–95.

Mukherjee, R., Gomez, M., Jayaraman, N., Smith, I., and Chatterji, D. (2005). Hyperglycosylation of glycopeptidolipid of *Mycobacterium smegmatis* under nutrient starvation: structural studies. Microbiology *151*, 2385–2392.

Neelamegham, S., Aoki-Kinoshita, K., Bolton, E., Frank, M., Lisacek, F., Lütteke, T., O'Boyle, N., Packer, N.H., Stanley, P., Toukach, P., et al. (2019). Updates to the Symbol Nomenclature for Glycans guidelines. Glycobiology *29*, 620–624.

Ojha, A.K., Varma, S., and Chatterji, D. (2002). Synthesis of an unusual polar glycopeptidolipid in glucose-limited culture of *Mycobacterium smegmatis*. Microbiology (Reading, Engl.) *148*, 3039–3048.

Park, I.K., Hsu, A.P., Tettelin, H., Shallom, S.J., Drake, S.K., Ding, L., Wu, U.-I., Adamo, N., Prevots, D.R., Olivier, K.N., et al. (2015). Clonal Diversification and Changes in Lipid Traits and Colony Morphology in *Mycobacterium abscessus* Clinical Isolates. J. Clin. Microbiol. *53*, 3438–3447.

Pawlik, A., Garnier, G., Orgeur, M., Tong, P., Lohan, A., Le Chevalier, F., Sapriel, G., Roux, A.-L., Conlon, K., Honoré, N., et al. (2013). Identification and characterization of the genetic changes responsible for the characteristic smooth-to-rough morphotype alterations of clinically persistent *Mycobacterium abscessus*. Mol. Microbiol. *90*, 612–629.

Poole, J., Day, C.J., von Itzstein, M., Paton, J.C., and Jennings, M.P. (2018). Glycointeractions in bacterial pathogenesis. Nat Rev Microbiol *16*, 440–452.

Poole, J., Day, C.J., Haselhorst, T., Jen, F.E.-C., Torres, V.J., Edwards, J.L., and Jennings, M.P. (2020). Repurposed Drugs That Block the Gonococcus-Complement Receptor 3 Interaction Can Prevent and Cure Gonococcal Infection of Primary Human Cervical Epithelial Cells. MBio *11*.

Richard, M., Gutiérrez, A.V., Viljoen, A., Rodriguez-Rincon, D., Roquet-Baneres, F., Blaise, M., Everall, I., Parkhill, J., Floto, R.A., and Kremer, L. (2019). Mutations in the MAB_2299c TetR Regulator Confer Cross-Resistance to Clofazimine and Bedaquiline in *Mycobacterium abscessus*. Antimicrob. Agents Chemother. *63*.

Ripoll, F., Deshayes, C., Pasek, S., Laval, F., Beretti, J.-L., Biet, F., Risler, J.-L., Daffé, M., Etienne, G., Gaillard, J.-L., et al. (2007). Genomics of glycopeptidolipid biosynthesis in *Mycobacterium abscessus* and *M. chelonae*. BMC Genomics *8*, 114.

Roux, A.-L., Ray, A., Pawlik, A., Medjahed, H., Etienne, G., Rottman, M., Catherinot, E., Coppée, J.-Y., Chaoui, K., Monsarrat, B., et al. (2011). Overexpression of proinflammatory TLR-2-signalling lipoproteins in hypervirulent mycobacterial variants. Cell. Microbiol. *13*, 692–704.

Roux, A.-L., Viljoen, A., Bah, A., Simeone, R., Bernut, A., Laencina, L., Deramaudt, T., Rottman, M., Gaillard, J.-L., Majlessi, L., et al. (2016). The distinct fate of smooth and rough *Mycobacterium abscessus* variants inside macrophages. Open Biol *6*.

Roy, R., Murphy, P.V., and Gabius, H.-J. (2016). Multivalent Carbohydrate-Lectin Interactions: How Synthetic Chemistry Enables Insights into Nanometric Recognition. Molecules *21*.

Ryan, K., and Byrd, T.F. (2018). *Mycobacterium abscessus*: Shapeshifter of the Mycobacterial World. Front Microbiol *9*.

Schlesinger, L.S., Hull, S.R., and Kaufman, T.M. (1994). Binding of the terminal mannosyl units of lipoarabinomannan from a virulent strain of *Mycobacterium tuberculosis* to human macrophages. J Immunol *152*, 4070–4079.

Shepherd, V.L., Stahl, P.D., Bernd, P., and Rabinovitch, M. (1983). Receptor-mediated entry of beta-glucuronidase into the parasitophorous vacuoles of macrophages infected with *Leishmania mexicana* amazonensis. Journal of Experimental Medicine *157*, 1471–1482.

Stover, C.K., de la Cruz, V.F., Fuerst, T.R., Burlein, J.E., Benson, L.A., Bennett, L.T., Bansal, G.P., Young, J.F., Lee, M.H., and Hatfull, G.F. (1991). New use of BCG for recombinant vaccines. Nature *351*, 456–460.

Thornton, B.P., Větvicka, V., Pitman, M., Goldman, R.C., and Ross, G.D. (1996). Analysis of the sugar specificity and molecular location of the beta-glucan-binding lectin site of complement receptor type 3 (CD11b/CD18). J Immunol *156*, 1235–1246.

Turner, J., and Torrelles, J.B. (2018). Mannose-capped lipoarabinomannan in *Mycobacterium tuberculosis* pathogenesis. Pathog Dis *76*.

Van Overtveldt, S., Gevaert, O., Cherlet, M., Beerens, K., and Desmet, T. (2018). Converting Galactose into the Rare Sugar Talose with Cellobiose 2-Epimerase as Biocatalyst. Molecules *23*.

Viljoen, A., Blaise, M., de Chastellier, C., and Kremer, L. (2016). MAB_3551c encodes the primary triacylglycerol synthase involved in lipid accumulation in *Mycobacterium abscessus*. Mol Microbiol *102*, 611–627.

Viljoen, A., Gutiérrez, Ana Victoria, Dupont, C., Ghigo, E., and Kremer, L. (2018). A simple and rapid gene disruption strategy in *Mycobacterium abscessus*: on the design and application of glycopeptidolipid mutants. Front. Cell. Infect. Microbial. *8:69*.

Viljoen, A., Viela, F., Kremer, L., and Dufrêne, Y.F. (2020). Fast chemical force microscopy demonstrates that glycopeptidolipids define nanodomains of varying hydrophobicity on mycobacteria. Nanoscale Horiz *5*, 944–953.

Villeneuve, C., Etienne, G., Abadie, V., Montrozier, H., Bordier, C., Laval, F., Daffe, M., Maridonneau-Parini, I., and Astarie-Dequeker, C. (2003). Surface-exposed glycopeptidolipids of *Mycobacterium smegmatis* specifically inhibit the phagocytosis of mycobacteria by human macrophages. Identification of a novel family of glycopeptidolipids. J Biol Chem *278*, 51291–51300.

Villeneuve, C., Gilleron, M., Maridonneau-Parini, I., Daffé, M., Astarie-Dequeker, C., and Etienne, G. (2005). Mycobacteria use their surface-exposed glycolipids to infect human macrophages through a receptor-dependent process. J Lipid Res *46*, 475–483.

Wagstaff, B.A., Zorzoli, A., and Dorfmueller, H.C. (2021). NDP-rhamnose biosynthesis and rhamnosyltransferases: building diverse glycoconjugates in nature. Biochemical Journal *478*, 685–701.

Whang, J., Back, Y.W., Lee, K.-I., Fujiwara, N., Paik, S., Choi, C.H., Park, J.-K., and Kim, H.-J. (2017). *Mycobacterium abscessus* glycopeptidolipids inhibit macrophage apoptosis and bacterial spreading by targeting mitochondrial cyclophilin D. Cell Death Dis *8*, e3012.

Woods, G.L., Brown-Elliott, B.A., Conville, P.S., Desmond, E.P., Hall, G.S., Lin, G., Pfyffer, G.E., Ridderhof, J.C., Siddiqi, S.H., Wallace, R.J., et al. (2011). Susceptibility Testing of Mycobacteria, Nocardiae, and Other Aerobic Actinomycetes (Wayne (PA): Clinical and Laboratory Standards Institute).

Xia, Y., and Ross, G.D. (1999). Generation of recombinant fragments of CD11b expressing the functional beta-glucan-binding lectin site of CR3 (CD11b/CD18). J Immunol *162*, 7285–7293.

Zelensky, A.N., and Gready, J.E. (2005). The C-type lectin-like domain superfamily. FEBS J *272*, 6179–6217.

FIGURE LEGENDS

Figure 1. GPL composition characterizing the *gtf* mutants.

(A) Structure of methoxylated GPL-3. The Symbol Nomenclature for Glycans (SFNG) is used throughout the figure to symbolize monosaccharides (Neelamegham et al., 2019). X represents the branched-chain amino-alcohol, alaninol or valinol. The lipid moiety is made of a combination of saturated and unsaturated β-methoxylated fatty acids.

(B) TLC profiles of GPL isolated from WT *M. abscessus* S and R strains, the single deletion mutants *gtf1* (Δ1), *gtf2* (Δ2) and *gtf3* (Δ3) as well as their complemented counterparts (Δ1_C, Δ2_C and Δ3_C) and multiple *gtf* deletion mutants (Δ1,2; Δ1,3; Δ2,3; Δ1,2,3). WT profiles were restored in all complemented strains. TLC plates were developed in $CHCl_3/CH_3OH/H_2O$ (90/10/1, v/v/v), stained with orcinol reagent and charred.

(C) Monosaccharide composition (expressed as the proportion of each monosaccharide) shows the absence of deoxy hexoses in *M. abscessus* R while deletion of *gtf1* or *gft3* induces the disappearance of 3(CH_3)Rha and 6-dTal or Rha, respectively. No deoxy hexose was observed in Δ2, similarly to *M. abscessus* R.

(D) MALDI-TOF-MS spectra of GPL from *M. abscessus* strains. The R variant is dominated by Ac_1PIM_2 signal whereas the S variant shows two heterogenous clusters of major signals at *m/z* 1258/1286 and 1404/1432, tentatively identified as $[M+Na]^+$ adducts of diglycoylsated (GPL-2a) and triglycosylated (GPL-3) GPL, respectively. Single *gtf* deletions induced drastic changes in the GPL profiles, as shown in the spectra.

(E) MALDI-TOF-MS^2 spectrum of WT GPL-3 parent ion at *m/z* 1432, confirms the respective positions of monosaccharides on the peptide moiety.

(F) MALDI-TOF-MS^2 spectrum of wild-type GPL-2a parent ion at *m/z* 1286 shows the absence of the external Rha.

Figure 2. Proposed pathway for *M. abscessus* GPL glycosylation.

(A) The presence of different GPL glycoforms found in WT and *gtf* mutants was evaluated by TLC and confirmed by MS. While GPL-1a has not been confirmed in any of the *gtf* mutants, all other glycoforms (GPL-1a, GPL-1b, GPL-2a, GPL-2b and GPL-3) were detected at specific *m/z* as native or saponified GPL and assigned in the different mutants.

(B) The glycosylation biosynthetic pathway of GPL in *M. abscessus* was modeled based on the distribution of individual GPL in the *gtf* mutants. First, Gtf2 adds the internal Rha to the branched chain amino-alcohol of the peptidolipid core, resulting in GPL-1b. Second, Gtf1 and Gtf3 add the 6-dTal and the external Rha residue, resulting in GPL-2b and GPL-2a, respectively. The combined action of all three enzymes generates GPL-3.

Figure 3. Deletion of *gtf* genes alters colonial morphology, hydrophobicity, sliding motility and biofilm formation.

(A) Knock-out of *gtf1* or *gtf2,* but not *gtf3,* is associated with rough and corded colonies, similar to the WT R reference strain. The various *M. abscessus* strains were grown on Tryptic Soy agar plates and incubated at 37° C for 5 days.

(B) Gtf1 and Gtf2 maintain a normal hydrophilicity index of the smooth morphotype. *M. abscessus* R, Δ1, Δ2, double and triple mutants and Gtf3 overexpressing strain are more hydrophobic than S, while the Δ3 and Δ*fmt* mutants hydrophilicity is significantly higher than S, as assessed by hexadecane partitioning and shown as the hydrophobicity index (in percentage of aqueous phase OD prior to partitioning). Histograms and error bars are means ± SD of four independent experiments (each time in triplicate) (n=12). Differences between means were analyzed for significance using a two-tailed Student's t-test employing Welch's correction for unequal variances. ns, non-significant; ***p < 0.001.

(C) Disruption of *gtf1* and/or *gtf2* genes reduces the sliding motility distance traveled by *M. abscessus* strains. Smooth morphotype strains slide more than R variants. Quantification of sliding ability. The sliding distances were measured in mm and plotted. Histograms and error bars are means ± SD of six independent experiments (each time in triplicate) (n=18). Data were analyzed with one-way ANOVA and Tukey's multiple comparison. ns, non-significant; **p < 0.01; ***p < 0.001.

(D) The absence of Gtf1 and Gtf2 promotes biomass formation at the air-liquid interface in *M. abscessus*. The rough variants of *M. abscessus* develop more significant biofilm structures at the air-liquid interface than the smooth variants. Biomass (expressed as CV absorbance) was greater with the rough strains than with the smooth variants. Histograms and error bars are means ± SD of three independent experiments (each time in sextuplicate) (n=24). Data were analyzed with one-way ANOVA and Tukey's multiple comparison. ns, non-significant; **p < 0.01; ***p < 0.001. See also Figure S4.

(E) The knock-out of *gtf1* and/or *gtf2* genes impairs biomass formation at the solid/liquid interface in *M. abscessus*. Smooth variants of *M. abscessus* evolve more important biofilm structures at the solid/liquid interface than rough morphotype strains. To assess the biomass development of each strain at the solid/liquid interface, 6-day-old *M. abscessus* biofilms were enumerated for CFUs. Data are mean values ± SD for three independent experiments (each time in quadruplicate) (n=12). One-tailed Mann–Whitney test: ns, non-significant; ***p < 0.001. See also Figure S4.

Figure 4. *Δgtf1* and *Δgtf2* mutants lead to large extracellular cord and abscess formation in a zebrafish embryo model.

(A) Embryos at 30 hours post-fertilization were infected with ~250-300 CFU of *M. abscessus via* caudal vein injection and survival was monitored daily over a 12 day-period. Statistical analysis was performed using the log-rank (Mantel-Cox) statistical test for survival analysis.

(B) The presence of cords in each embryo was quantified via fluorescent microscopy at 2- and 4-day post-infection.

(C) The number of cords per embryo was further quantified using fluorescent microscopy at 2- and 4-days post-infection.

(D) The proportion of embryos with abscesses was identified using fluorescent microscopy at 2-, 4- and 6-days post-infection.

(E) The number of abscesses per embryo was quantified with fluorescent microscopy at 2-, 4- and 6-days post-infection. Statistical analysis for cord and abscess quantification was performed using unpaired students t-tests.

(F) Representative images of each *M. abscessus* strain expressing the pTEC27 fluorescent plasmid in zebrafish embryos at 4 days post-infection. Values for all data displayed are the mean ± standard deviation with the merge of three independent experiments. $P \leq 0.05$, ** ≤ 0.01, *** $P \leq 0.001$.

Figure 5. Internalization of *M. abscessus* by macrophages requires glycosylated GPL.

(A) Intracellular bacterial load is reduced in macrophages infected with single, double or triple *gtf* mutants. CFU were determined at hours 3, 24, and 72 post-infection. Data are mean values ± SD for ten independent experiments (each time in triplicate) (n=30). One-tailed Mann−Whitney test: ns, nonsignificant; ***p < 0.001.

(B) The percentage of infected macrophages decreased when cells were infected with single, double or triple *gtf* mutants. Percentage of infected THP-1 macrophages at hours 3, 24, and 72 post-infection. Data are mean values ± SD for three independent experiments (each time in triplicate) (n=180). One-tailed Mann−Whitney test: ns, non-significant; ***p < 0.001.

(C) Twelve immunofluorescent fields were taken after 24 hours post-infection at a 40X magnification (using a confocal microscope), showing the macrophages infected with the various strains (in red). The nuclei are shown in blue, the CD43 protein associated with the plasma membrane and present on the surface of macrophages is stained in green. White arrows indicate mycobacteria within the macrophages. Scale bars represent 20 µm.

(D) The number of bacilli per infected macrophage declines when cells are infected with single, double or triple *gtf* mutants. Analysis of the percentage of macrophage categories infected with different numbers of bacilli. The first image illustrates a macrophage containing fewer than 5 bacilli, the second encompasses 5 to 10 bacilli, and the third comprises >10 bacilli (right panels). The surface of macrophages was detected using anti-CD43 antibodies (green). The nuclei were stained with DAPI (blue). The macrophage categories were counted at 3 hpi (left panel). The percentages of macrophages containing different numbers of bacilli (0−5, 5−10, and >10) are represented on the y axis. Values are means ± SD for three independent experiments performed each time in triplicate (n=900 infected macrophages). Data were analyzed using the one-tailed nonpaired t test. ns, non-significant; ***p < 0.001.

Figure 6. Triglycosylated GPL favors colonization of macrophages by *M. abscessus.*

(A) Overexpression of Gtf3-HA in *M. abscessus*. The *gtf3* gene was fused to HA and cloned into the integrative vector pMV306 (lane 3) or episomal pMV261 (lane 4) allowing its expression under the control of its native promoter (in Δ3 strain) or hsp60 (in the wild-type smooth strain) respectively. Western blot analysis of Gtf3 expression in the complemented Δ3 strain or its overexpression in the wild-type S morphotype strain using anti-HA antibodies (upper panel). The KasA protein (probed with anti-KasA antibodies) was used as a loading control (lower panel).

(B) GPL-2 and GPL-3 accumulated in Δ3, and Gtf3_ov strains respectively. TLC analysis of the crude lipid fractions of the smooth, Δ3 mutant, Δ3 complemented and Gtf3 overexpressing strains. GPL-2 and GPL-3 were separated using a solvent composed of CHCl3/MeOH (9:1, v/v) and revealed with orcinol staining after one round of migration.

(C and D) Overexpression of Gtf3 leading to accumulation of GPL-3 enhances entry of bacilli into THP-1 and primary human macrophages. CFU were determined at hours 3 (C and D), 24 (C), and 72 (C) post-infection. Data are mean values ± SD for three independent experiments (each time in pentaplicate (C) or quadruplicate (D)) (n=15 (C) or 12 (D)). One-tailed Mann−Whitney test: ns, non-significant; ***p < 0.001.

(E) Two immunofluorescent fields were taken after 24 hours post-infection at a 40X magnification (using a confocal microscope), showing the macrophages infected with the various strains (in red). The nuclei are shown in blue and the CD43 protein is stained in green. White arrows indicate mycobacteria within the macrophages. Scale bars represent 20 µm.

(F) The percentage of infected macrophages augmented when cells were infected with Gtf3_ov strain. Percentage of infected THP-1 macrophages at hours 3, 24, and 72 post-infection. Data are mean values ± SD for three independent experiments (each time in triplicate) (n=60 fields). One-tailed Mann−Whitney test: ns, non-significant; ***p < 0.001.

(G) The number of bacilli per infected macrophage upsurges when cells are infected with Gtf3_ov strain. Analysis of the percentage of macrophage categories infected with different numbers of bacilli. The macrophage categories were counted at hours 3, 24, and 72 post-infection. The percentages of macrophages containing different numbers of bacilli (0−5, 5−10, and >10) are represented on the y axis. Values are means ± SD for three independent experiments performed each time in triplicate (n=900 infected macrophages). Data were analyzed using the one-tailed nonpaired t test. ns, non-significant; **p < 0.01.

(H) Increased invasion of the strain that overexpresses Gtf3 is reduced in macrophages pretreated with mannan, laminarin and methyl-α-D-glucopyranoside. Intracellular bacterial load is significantly reduced in macrophages pretreated with the 3 compounds mentioned above and infected specifically with the strain that overexpresses Gtf3. CFU were determined at 3 hpi. Data are mean values ± SD for four independent experiments (each time in triplicate) (n=12). One-tailed Mann−Whitney test: ***p < 0.001.

Figure 7. Triglycosylated GPL-conjugated beads are efficiently phagocytosed by macrophages and internalization depends on MR and CR3 receptors.

(A) Representative fluorescent images showing the efficiency of internalization of GPL-3-coupled beads by macrophages. CD43 (red), DAPI (blue), fluorescent beads (green). White arrows indicate fluorescent beads within the macrophages. Scale bars represent 20 µm. See also Figure S7.

(B) Beads ingestion is optimal only when they are coupled to the triglycosylated form of GPL. Quantification of the percentage of THP-1 containing beads was determined after 4 hours. The beads alone were used as a negative control. The ratio of beads per macrophage was 10:1. Data are mean values ± SD for three independent experiments (each time in triplicate) (n=60 fields). One-tailed Mann−Whitney test: ns, non-significant; ***$p < 0.001$.

(C) On average, macrophages ingest twice as many beads coupled to GPL-3. Quantification of the average number of beads per macrophage was set on after 4 hours of phagocytosis. Data are mean values ± SD for three independent experiments (each time in triplicate) (n=900 macrophages containing beads). One-tailed Mann−Whitney test: ns, non-significant; ***$p < 0.001$.

(D) Blocking both MR and CR3 receptors significantly reduces cell colonization by beads coupled to both GPL-2a and GPL-3. No significant inhibition of phagocytosis was observed when the pre-treated macrophages were incubated in presence of beads alone or coupled to GPL-1b and GPL-2b. Quantification of the percentage of THP-1 containing beads was determined after 4 hours. Data are mean values ± SD for three independent experiments (each time in triplicate) (n=60 fields). One-tailed Mann−Whitney test: ns, nonsignificant; ***$p < 0.001$. See also Figure S7.

(E) Representative fluorescent images showing the impact of neutralizing anti-MR and/or anti-CR3 antibodies on the internalization of GPL-2a and/or GPL-3 beads by macrophages. CD43 (red), DAPI (blue), fluorescent beads (green). White arrows indicate the presence of fluorescent beads inside macrophages. Scale bars represent 20 µm. See also Figure S7.

(F) Blocking MR or CR3 receptors with neutralizing antibodies significantly reduced cell colonization by beads coupled to GPL-2a and GPL-3. Quantification of the percentage of THP-1 containing beads was determined after 4 hours. Data are mean values ± SD for three independent experiments (each time in triplicate) (n=180 fields). One-tailed Mann-Whitney test: ***$p < 0.001$. See also Figure S7.

(G) Macrophages pretreated with neutralizing antibodies ingested less beads coupled to GPL-2a (anti-MR) or GPL-3 (anti-MR and anti-CR3) than the non-treated control beads. Quantification of the number of beads per macrophage was performed after 4 hours of phagocytosis. The red bar in each violin plot represents median. The colored area of a violin plot corresponds to the probability density of the data and contains first and third quartiles. Data are mean values ± standard deviation from three independent experiments (each time in triplicate) (n=900 macrophages containing beads per condition). One-tailed Mann-Whitney test: *$p < 0.05$; ***$p < 0.001$.

STAR★METHODS

KEY RESOURCES TABLE

REAGENT or RESOURCE	SOURCE	IDENTIFIER
Experimental Model: Bacterial Strains		
Mycobacterium abscessus sensu stricto, strain CIP104536^T, smooth	Laboratoire de Référence des Mycobactéries (IP, France)	ATCC19977^T
Mycobacterium abscessus sensu stricto, strain CIP104536^T, rough	Laboratoire de Référence des Mycobactéries (IP, France)	ATCC19977^T
Δ1: Unmarked deletion of *gtf1* in *M. abscessus* S	This study	N/A
Δ1 + pMV306-*gtf1 :* Δ1 carrying pMV306-*gtf1*	This study	N/A
Δ2: Unmarked deletion of *gtf2* in *M. abscessus* S	This study	N/A
Δ2 + pMV306-*gtf2 :* Δ2 carrying pMV306-*gtf2*	This study	N/A
Δ3: Unmarked deletion of *gtf3* in *M. abscessus* S	This study	N/A
Δ3 + pMV306-*gtf3 :* Δ3 carrying pMV306-*gtf3*	This study	N/A
S + pMV261-*gtf3 :* S carrying pMV261-*gtf3*	This study	N/A
Δ1,2: Unmarked deletions of *gtf1* and *gtf2* in *M. abscessus* S	This study	N/A
Δ1,3: Unmarked deletions of *gtf1* and *gtf3* in *M. abscessus* S	This study	N/A
Δ2,3: Unmarked deletions of *gtf2* and *gtf3* in *M. abscessus* S	This study	N/A
Δ1,2,3: Unmarked deletions of *gtf1* and *gtf2* and *gtf3* in *M. abscessus* S	This study	N/A
E. coli XL1-Blue	*recA1 endA1 gyrA96 thi-1 hsdR17 supE44 relA1 lac* [F´ *proAB lacI*q*ZΔM15* Tn*10* (Tetr)]	Stratagene
Oligonucleotides		
Primers used in this study are listed in Table S1		
Zebrafish line		
golden mutant	(Lamason et al., 2005)	N/A
Chemicals, Enzymes and kits		
Hygromycin B	Sigma-Aldrich	Cat#H3274
Kanamycin	Euromedex	Cat#EU0420-B
Difco Middlebrook 7H9 Broth	Thermo Fisher Scientific	Cat#DF0713-17-9
Middlebrook OADC Growth Supplement	Sigma-Aldrich	Cat#M0678
Tween-80	Sigma-Aldrich	Cat#P1754
Q5 DNA Polymerase	New England Biolabs	Cat#M0491L
T4 DNA Ligase	New England Biolabs	Cat#M0202S
NucleoSpin Plasmid Kit	Machery-Nagel	Cat#740588.50
NucleoSpin Gel and PCR Clean-up	Machery-Nagel	Cat#740609.50

GenElute HP Plasmid Midiprep Kit	Sigma-Aldrich	Cat#NA0200-1KT
Laminarin	Sigma-Aldrich	Cat#L9634-100MG
Mannan	Sigma-Aldrich	Cat#M7504-250MG
Methyl α-D-GLUCOPYRANOSIDE	Sigma-Aldrich	Cat#M9376-100G
Super Signal West Femto Maximum Sens	Life-Technologies	Cat#34095
Plasmids		
pTEC27 (Multicopy *E. coli*/mycobacterial shuttle vector expressing *tdTomato* under the control of a strong mycobacteri promoter)	Addgene	Cat#30182
pUX1-*katG* (Variant of *pUX1* containing the *katG* gene of *M. tuberculosis* as a counter-selectable marker in the presence of INH and used for the generation of unmarked chromosomal alterations)	(Richard et al., 2019)	N/A
pMV306 (*E. coli*/mycobacterial integrative vector)	(Stover et al., 1991)	N/A
pMV261 (Multi-copy *E. coli*/mycobacterial shuttle vector. Cloned genes are under the control of the constitutive *hsp60* promoter)	(Stover et al., 1991)	N/A
Software and Algorithms		
Prism 9.0	Graphpad	https://www.graphpad.com
Fiji (ImageJ)	NIH	https://fiji.sc
Zen (Blue edition)	Zeiss	https://www.zeiss.com/microscopy/int/products/microscope-software/zen.htmL
Imaris	Oxford	https://imaris.oxinst.com
Biological samples and Cell Lines		
Primary human monocyte-derived macrophages from human blood (Buffy coats)	Etablissement Français du Sang (EFS), Montpellier, France	N/A
THP-1 macrophages	This paper	ATCC® TIB-202™
Antibodies		
Rat anti-HA (3F10)	Merck	Cat#11867423001
Rat anti-KasA	(Viljoen et al., 2016)	N/A
Mouse anti-HU CD11B	Life Technologies	Cat#4-0118-82
Mouse anti-HU CD206	Becton Dickinson	Cat#555953
Mouse anti-HU CD43	Becton Dickinson	Cat#555474
Mouse IgG1	Becton Dickinson	Cat#555746
Mouse anti-HU Dectin-1	InvivoGen	Cat#mabg-hdect
Alexa Fluor 488 anti-Mouse IgG (Goat)	Life Technologies	Cat#A11017
Alexa Fluor 594 anti-Mouse IgG (Goat)	Life Technologies	Cat#A11032
Anti-Rat IgG H&L (HRP) (Goat)	Abcam	Cat#ab97057
CCM analysis		
TLC plate	Macherey Nagel	Cat#818333
Chloroform	Carlo	Cat#412652
Methanol	VWR	Cat#20864.320
Orcinol	Sigma	Cat#O1875
Phosphomolybdic acid	Sigma	Cat#78560
GC analysis		
6-deoxy L-Talose	Carbosynth	Cat#MD04657

L-Rhamnose monohydrate	Carbosynth	Cat#MR00035
SOLGEL 1-MS	SGE	Cat#054795
MALDI TOF analysis		
Super DHB	Sigma	Cat#50862
RMN analysis		
CDCl3	Eurisotop	Cat#D007H
CD3OD	Eurisotop	Cat#D048B
Purification		
Silica column	Interchim	Cat#FF-15SIHP-F0004
TLC plate	Macherey Nagel	Cat#809061
Coating		
Fluospheres	Thermo Fisher Scientific	Cat#F8852
Carbonate	Sigma	Cat#S7795
Bicarbonate	Sigma	Cat#S5761
Butanol	VWR	Cat#83633.290
Phosphate Buffer Saline	Euromedex	Cat#ET330
Bovine Serum Albumin	Sigma	Cat#A0281

CONTACT FOR REAGENT AND RESOURCE SHARING

Further information and requests for resources and reagents should be directed to and will be fulfilled by the Lead Contact, Laurent Kremer, (laurent.kremer@irim.cnrs.fr).

EXPERIMENTAL MODELS AND SUBJECT DETAILS

Mycobacterial strains, growth conditions and reagents

All bacterial strains are listed in key resources table. Rough (R) and smooth (S) variants of *M. abscessus* CIP104536^T were typically grown in Middlebrook 7H9 broth (BD Difco) supplemented with 0.05% Tween 80 and 10% oleic acid, albumin, dextrose, catalase (OADC enrichment; BD Difco) (7H9$^{T/OADC}$) at 37°C in the presence of antibiotics, when required. Electrocompetent mycobacteria were transformed using a Bio-Rad Gene pulser (25 µF, 2500 V, 800 Ohms). For bacterial selection, media were supplemented either with 1 mg/mL hygromycin for strains carrying pTEC27 (Addgene, plasmid 30182), allowing tdTomato expression, or with 250 µg/mL kanamycin when harboring the pMV306 or pMV261 derivatives. On plates, colonies were selected either on Middlebrook 7H10 agar (BD Difco) supplemented with 10% OADC enrichment (7H10^{OADC}) or on LB agar or on Tryptic Soy Broth agar (Sigma). Antibiotics were purchased from Sigma-Aldrich.

In vitro growth, sliding motility and sedimentation assays

Growth was inspected by inoculating the mid-log phase cultures into fresh 7H9 at an OD_{600} of 0.05. Cultures were incubated at 37° C with shaking and OD600 was monitored for 144 hrs using a Synergy H1 hybrid reader (BioTek). To visualize colony morphology, bacteria from log phase cultures (OD_{600} = 1) were resuspended in phosphate buffered saline (PBS) and 2 µL of the cell suspension was spotted onto Tryptic Soy Broth agar. Plates were then incubated for 5 days at 37° C and colonies were imaged using a Zeiss microscope equipped with a Zeiss Plan Neo Fluor Z1×/0.25 FWD objective. Images were acquired with an Axiocam503 monochrome

(Zeiss) camera and processed using ZEN 2 (blue edition). Sliding motility was examined as previously described (Bernut et al., 2016). *M. abscessus* were inoculated on 7H9 with 0.3% agar and 6 days of incubation at 37° C, the sliding distance was measured using ImageJ. For sedimentation experiments, cultures were diluted to an OD_{600} of 1 and 2 mL of culture were transferred to a glass tube. Images were taken after 5 min.

Biofilm assays

Pellicle formation was assessed by inoculating 10 µL of mid-log phase cultures onto M63 medium supplemented with 10% glucose, 1 mM $CaCl_2$ and 1 mM $MgSO_4$, and the samples were incubated for 6 days at 30°C without agitation. To quantify biofilm production at the liquid/air and solid/liquid interfaces, 10 µL of mid-log phase cultures were deposited on the surface of M63 broth (6 mL) in glass tubes. After 6 days of incubation at 37° C, biofilms were visible at the liquid/air interface but also at the bottom of the glass tubes. Biomasses at the bottom of the tubes were collected with M63 medium and after centrifugation and removal of the supernatant, bacterial pellets were suspended in 1 mL PBS, diluted and finally spread on LB agar medium. After 5 days of incubation at 37° C, the CFU were counted. The biofilms at the liquid/air interface were stained with 1 mL of 0.1% (w/v) crystal violet in 20% (v/v) ethanol/water for 30 min. The excess stain was washed with four consecutive PBS washes and the remaining crystal violet was solubilized in 30% acetic acid and absorbance measured at 570nm.

Hexadecane partitioning

Exponentially-growing bacteria were washed twice in PUM buffer (100 mM K_2HPO_4, 54 mM KH_2PO_4, 30 mM urea, 0.8 mM $MgCl_2$) and suspended to an OD_{600} of 0.7. Aliquots (3 mL) were transferred to glass tubes and hexadecane (2.4 mL) was added. After a brief mixing, samples were incubated for 8 min at 37° C and phase separation was allowed to occur for 15 min at 22° C. The hydrophobicity index was defined as aqueous phase at OD_{600}, expressed as a percentage of that of the bacterial suspension in PUM buffer alone (Jankute et al., 2017).

Deletion of *gtf* genes in *M. abscessus*

The suicide vector pUX1-*katG* was used to generate unmarked single, double and triple deletion mutants in *M. abscessus* CIP104536^T (S). Briefly, the left and right arms (LA and RA, respectively) were PCR-amplified using genomic DNA and Q5 polymerase (New England Biolabs) as well as primers 1/2, 5/6, and 9/10 (LA) and primers 3/4, 7/8, and 11/12 (RA) **(Table S1)**. The purified LA and RA amplicons were restricted with PacI/MfeI and MfeI/NheI, respectively, and ligated to the PacI/NheI-linearized pUX1-*katG*, yielding pUX1-*katG-gtf1*, pUX1-*katG-gtf2* and pUX1-*katG-gtf3,* designed to delete 1182 bp (93%), 1104 bp (88%), and 1113 bp (84%) of the *gtf1* or *gtf2* or *gtf3* open reading frames, respectively. Electrocompetent *M. abscessus* was transformed with pUX1-*katG-gtf1*, pUX1-*katG-gtf2* and pUX1-*katG-gtf3* to generate the single mutants. Δ3

was subsequently used to generate the Δ1,3 and Δ2,3 double mutants. The Δ1,2 and Δ1,2,3 strains were derived from Δ1 and Δ1,3, respectively. The selection of bacteria having undergone the first homologous recombination event was done by visual screening of red fluorescent colonies on $7H10^{OADC}$ supplemented with 250 µg/mL kanamycin. After subculturing the culture overnight in $7H9^{T/OADC}$ in the absence of kanamycin, bacterial suspensions were serially diluted and plated onto $7H10^{OADC}$ with 50 µg/mL INH to select for INH-resistant, Kan-sensitive and non-fluorescent colonies. The DNA junctions were PCR sequenced to confirm the genotypes of the appropriate mutants using primers listed in **Table S1**.

Complementation and overexpression of Gtf3 in *M. abscessus.*

Complementation plasmids were generated by PCR amplifying the *gtf1*, *gtf2* and *gtf3* genes in fusion with an HA-tagging sequence under the control of the *hsp60* promoter (for *gtf1*) or of their endogenous promoters (175 bp for *gtf2* and 500 bp for *gtf3*) using genomic DNA and the forward 19/21/23 and reverse primers 20/22/24 (containing the HA-coding sequence) and ligation into the integrative pMV306 cut with the appropriate restriction enzymes **(Table S1)**, yielding pMV306-*gtf1*, pMV306-*gtf2* or pMV306-*gtf3*. All constructs were verified by DNA sequencing and introduced into Δ1, Δ2 or Δ3. Overexpression was achieved by PCR amplification of *gtf3* in fusion with an HA tag using genomic DNA and the forward primer (25; MscI) and reverse primer (26; EcoRI). The amplicon was digested with MscI/EcoRI and ligated into the MscI/EcoRI-restricted multicopy pMV261 to generate pMV261-*gtf3*-HA. The construct was sequenced and introduced in WT S.

Western blotting

Bacteria were harvested, resuspended in PBS, and disrupted by bead beating using 1 mm diameter glass beads. Protein concentration was assessed using the BCA Protein Assay Reagent kit (Pierce), according to the manufacturer's instructions. Equal amounts of proteins (50 µg) were separated by SDS/PAGE and transferred to a nitrocellulose membrane. For detection of Gtf1-HA, Gtf2-HA, Gtf3-HA and KasA (loading control), membranes were probed for 1 hr with either rat anti-HA (Sigma) or rat anti-KasA antibodies (Viljoen et al., 2016) (dilution 1:2000). After washing, membranes were incubated for 45 min with goat anti-rat antibody conjugated to HRP (dilution 1:5000; Abcam) and bands revealed using the ChemiDoc MP system (Bio-Rad laboratories).

Drug susceptibility testing

The MICs were determined according to the CLSI guidelines (Woods et al., 2011). The broth microdilution method was used in CaMHB with an inoculum of $5x10^6$ CFU/mL in the exponential growth phase. The bacterial suspension was seeded in 100 µL volumes in all of the wells of a 96-well plate, except for the first column, to which 198 µL of the bacterial suspension was added. In the first column, 2 µL of drug at its highest

concentration was added to the first well containing 198 µL of bacterial suspension. Then, 2-fold serial dilutions were carried out, and the plates were incubated for 5 days at 30°C. MIC were recorded by visual inspection. Assays were completed in triplicate in three independent experiments.

Zebrafish infection experiments

Zebrafish experiments were completed under European Union guidelines for the handling of laboratory animals and was approved by the Direction Sanitaire et Vétérinaire de l'Hérault and Comité d'Ethique pour l'Expérimentation Animale under reference 2020022815234677. Zebrafish infections were completed as previously described (Bernut et al., 2014a, 2015). Briefly, embryos at 30 hours post-fertilization were dechorionated and anaesthetized in tricaine prior to caudal vein injection with 2-3 nL of *M. abscessus* (~100 CFU/nL) expressing TdTomato fluorescent protein under the control of the pTEC27 plasmid. Following infection, embryos were recovered in fresh embryo water and placed in 24-well plates (2 embryos/well). Embryos were checked daily, with dead embryos removed from the well each day until 12 days post-infection. At 2-, 4- and 6-days post-infection, embryos were anaesthetized in tricaine and placed on 3% methylcellulose (w/v) for fluorescent microscopy using Zeiss Axio Zoom.V16 coupled with an Axiocam 503 mono (Zeiss). Bacterial cords were quantified based on size and shape of bacterial cords within the live zebrafish embryo, which was substantially larger in surrounding size and shape as compared to neighboring cells. Abscesses were quantified based on the large uncontrolled extracellular growth of fluorescent bacteria that exceeded 100 µm in diameter. All experiments displayed were performed in at least three independent experiments.

Macrophage infection assays

THP-1 macrophages were grown in RPMI medium supplemented with 10% fetal bovine serum (Sigma-Aldrich) and incubated at 37°C with 5% CO_2. THP-1 monocytes were differentiated in macrophages in the presence of 20 ng/mL phorbol myristate acetate in 24-well flat-bottom tissue culture microplates (10^5 cells/well) and incubated for 48 hrs at 37°C with 5% CO_2. Infection with *M. abscessus* strains (S, R, Δ1, Δ1C, Δ2, Δ2C, Δ3, Δ3C, Gtf3_ov, Δ1,2, Δ1,3, Δ2,3 and Δ1,2,3) carrying pTEC27 (MOI 2:1) was performed for 3 hrs at 37°C in the presence of 5% CO_2. Cells were carefully washed three times with 1× PBS and then incubated with $RPMI^{FBS}$ supplemented with 250 µg/mL amikacin for 2 hrs to kill extracellular bacteria. At various time points (3, 24, and 72 hpi), macrophages were washed three times with PBS and lysed with 100 µL of 1% Triton X100. Lysis was stopped by adding 900 µL PBS and serial dilutions were plated to monitor the intracellular bacterial counts. CFU were counted after 5 days of incubation at 37° C.

Immunofluorescence staining infected THP-1 macrophages

For microscopy-based infectivity assays, THP-1 cells were cultured on coverslips in 24-well plates at a density of 10^5 cells/well and incubated for 48 hrs at 37° C with 5% CO_2. Cells were infected with tdTomato-expressing *M. abscessus* (MOI 2:1) for 3 hrs, washed, treated with amikacin, fixed at 3, 24, and 72 hpi with 4% paraformaldehyde in PBS for 20 min permeabilized using 0.2% TritonX-100 for 20 min. After blocking with 2% BSA in PBS supplemented with 0.2% Triton X-100 for 20 min, cells were incubated with anti-CD43 antibody (Becton Dickinson; dilution 1:1000) for 1 hr and with a Alexa Fluor 488- or 594-conjugated anti-mouse secondary antibody (Molecular Probes, Invitrogen). Cells were then stained with 1 µg/mL 4',6-diamidino-2-phenylindole (DAPI; Becton Dickinson) for 5 min, washed with PBS, mounted onto microscope slides using Immumount (Calbiochem) and examined with either an epifluorescence microscope using a 63x lens objective or using a confocal microscope using a 40× objective (Zeiss LSM880). The average proportion of macrophages containing fewer than <5, 5−10, or >10 bacteria was quantified using Zeiss Axiovision software. Images were acquired by focusing on combined signals (CD43 in green and red fluorescent *M. abscessus*) and captured on a Zeiss Axioimager confocal microscope equipped with a 40x or 63× oil objective and processed using Zeiss Axiovision software. Scoring the number of bacilli present within macrophages were performed using ImageJ. Equal parameters for the capture and scoring of images were consistently applied to all samples.

Intra- and extracellular cords within or among the macrophages infected with the various R morphotype strains were imaged using confocal microscopy. High resolution confocal microscopy images were acquired with a LSM880 confocal microscope paired with an Airyscan module (ZEISS) with a 63x lens. The Zeiss LSM 880, Axio-Observer microscope is equipped with a Plan-Apochromat 63× Oil 1.4 NADIC M27 objective (Zeiss). The cords or macrophages containing green fluorescent beads were sectioned (mode Z-stacks) and slices were acquired every 0.18 µm, resulting in 38-42 serial slices per image. 3D imaging reconstruction of the 3D Airyscan confocal microscopy images was made with either Zen Black **(Figure S7A)** or IMARIS **(Figure S5)**. Each image channel was segmented individually by intensity thresholding and the final surface reconstruction was generated by an overlay of the three individual surfaces.

Infection of primary human monocyte-derived macrophages and intracellular CFU determination

Buffy coats from anonymous donors were obtained from the Etablissement Français du Sang (EFS), Montpellier, France. Peripheral blood mononuclear cells (PBMCs) were purified by Ficoll density gradient separation (Blanchet et al., 2010). Monocytes were isolated from PBMCs using a magnetic cell separation system with anti-CD14 mAb-coated microbeads (130-050-201; Miltenyi Biotec) and then cultured in complete IMDM supplemented with 50 ng/mL GM-CSF (every 2 days) at 37° C under a humidified 5% CO_2 atmosphere for 6 days. Cells were washed and detached with 20 mM EDTA in PBS and plated in a 24-well plate at a concentration of 10^5 cells/well with complete IMDM. Monocyte-derived macrophages were

infected with either S or Gtf3_ov strains for 3 hrs at a MOI of 2:1, washed, treated with 250 µg/mL amikacin for 2 hrs and replenished with fresh medium. To determine the number of internalized bacilli at 3 hpi, cells were lysed with 0.1% saponin and lysates plated on LB agar plates prior to CFU counting.

Fluorescent beads phagocytosis assay

The beads were added to the macrophages at a rate of 10 beads/cell. After 4 hrs of incubation at 37° C, macrophages were washed five times with PBS before labeling using anti-CD43 antibodies and Alexa Fluor 594-coupled anti-mouse secondary antibody. Quantification of the percentage of macrophages containing beads and the average number of beads per macrophage was done using an epifluorescence microscope.

Carbohydrate and antibody inhibition assays in macrophages

All carbohydrates (mannan, laminarin and methyl-α-D-glucopyranoside) were purchased from Sigma-Aldrich. For inhibition experiments, carbohydrates (100 µg/mL) were added to the cells for 1 hr in $RPMI^{FCS}$ medium prior to the addition of either the GPL-coupled beads or infection with the following strains: S, Δ1, Δ2, Δ3, Gtf3_ov and Δ1,3. Quantification of intracellular CFU and determination of the percentage of infected macrophages and average number of beads per macrophage was performed as described above. The antibody inhibition experiments were performed in a similar manner, except that the cells were incubated with the specific neutralizing antibodies in $RPMI^{FCS}$ medium for 3 hrs at a concentration of 50 µg/ml prior to determination of the percentage of macrophages that phagocytosed the beads and the average number of beads per macrophage.

Glycolipids extraction

GPL were extracted from bacteria grown on $7H10^{OADC}$ agar plates without detergent, first with chloroform/methanol/0.3%NaCl (9:10:3, v/v/v) and then by chloroform/methanol/0.3%NaCl (5:10:4, v/v/v). The combined solvent extracts were mixed for 5 min with chloroform and 0.3%NaCl (1:1, v/v) and centrifuged at 3,000 *g* for 5 min to separate the lower-organic phase from the aqueous phase. The upper aqueous layer was discarded and the lower-organic phase was evaporated under a stream of nitrogen and resuspended in chloroform/methanol (2:1, v/v). Apolar and polar lipids were subjected to TLC analysis using Silica gel 60 F_{254} plates (Merck). GPL were separated using chloroform/methanol/water (90:10:1, v/v/v) and PIMs using chloroform/acetic acid/methanol/water (40/25/6/3, v/v/v/v). Orcinol/sulfuric acid vapor was used to reveal glycolipids while phosphomolybdic acid/ethanol was preferred for peptidolipids.

GPL purification

2-Flash chromatography. The polar lipid fraction was impregnated with silica gel overnight. Impregnated silica was added on the top of a low-pressure silica gel column 15 µm, 4 g (INTERCHIM, France) and a linear gradient

was applied from 100 % chloroform to reach 85 % chloroform - 15 % methanol at 20 min using Puriflash (INTERCHIM, France). This ratio was maintained for 10 min. 6 mL fractions were collected and the presence of glycolipids was assayed by TLC. Fractions containing GPL were checked by MS then pooled, dried and dissolved in chloroform/methanol (2:1, v/v).

1-TLC. A second round of purification was performed: 150 µL of the GPL fraction was spotted on a 150 mm band on a 60 µm silica TLC plate with a glass back (20 cm x 20 cm) and migrated in a solution of chloroform/methanol/water (90:10:1, v/v/v). Plate sides were sprayed with orcinol/sulfuric acid and charred while the plate center was reversibly stained with iodide vapor to label lipids. GPL-containing silica was scraped and GPL were extracted in chloroform/methanol (2:1, v/v) under sonication for 1 hr. Silica was filtrated on glass wool and 0.2µm PTFE syringe filter. After TLC and MS analysis, purified GPL-1b was pooled from Δ1 and Δ1,3 while purified GPL-2a was prepared from Δ3 and WT *M. abscessus.* Purified GPL-2b was prepared from Δ1 and GPL-3 from WT *M. abscessus*.

Glycolipids saponification

10 µL of polar lipid fraction was dried under nitrogen, 200 µL sodium hydroxide 0.1 M in chloroform/methanol (2:1, v/v) was added and heated for 2 hrs at 37° C. After the reaction, 1 mL chloroform and 1 mL water were added. The mixture was agitated for 1 min then centrifuged for 30 sec. The lower chloroform phase was dried under nitrogen and dissolved in 150 µL chloroform/methanol (2:1, v/v).

Monosaccharides composition by GC/MS

For hydrolysis step, 1 µg mesoinositol, 20 µL GPL fraction and 1 mL trifluoroacetic acid 3 M were mixed then heated 4 hrs at 80° C and dried overnight. The reduction step was conducted for 4 hrs at room temperature in 500 µL $NaBH_4$ 10 mg/mL in 2 M NH_4OH. The reaction was stopped with dropwise addition of concentrated glacial acetic acid. Samples were dried at 55° C under a nitrogen stream by co-distillation with methanol/acetic acid three times, desiccated overnight and incubated in 500 µL anhydride acetic 4 hrs at 80° C. The reaction products were extracted three times with chloroform/water. The chloroform-rich phase was then filtered, dried and dissolved in 100 µL chloroform. 1 µL of monosaccharide derivatives was injected in splitless mode on a Solgel 1 MS 30 m x 0.25 mm x 0.25 µm capillary column with the following gradient temperature: 120° C to 230° C at 3° C/min, then to 270° C at 10° C/min. Compounds were detected after electronic impact at 70 eV on a HP-7820 gas chromatograph coupled to a 5976 single quad (Agilent Technologies, Santa Clara, US) in full scan mode from 50 Da to 500 Da. To quantify GPL prior to bead coating, similar experiments were conducted using 8 and 40 µg of Rha, 6-dTal and Man as external standards (Carbosynth, UK).

Bead coating

The protocol used was reported earlier (Schlesinger et al., 1994). Briefly, 15 µL containing $5.4.10^8$ of 1µm fluorescent (Em / Ex ; 505 nm / 515 nm) sulfate microspheres beads (THERMOFISHER SCIENTIFIC, San Jose, USA) were washed twice with 985 µL carbonate/bicarbonate 0.05M and resuspended in 1 mL PBS. Next to GC quantification, 40 µg of purified GPL were dissolved in 50 µL of water saturated butanol before adding 950 µL of beads in PBS. Coating was performed 2 hrs at 37° C under gentle agitation. Beads were washed twice with 1 mL PBS and blocked for 1 hr with 1 mL 5% BSA in PBS at 37 °C under gentle agitation. Beads were washed twice then transfer for storage at -20°C with 0.5% BSA in PBS. The detection of deoxyhexoses as trimethylsilyl derivatives in the preparation tube was negative. The bead shape was checked with confocal microscopy.

MALDI-TOF mass spectrometry

5 µL of 10 mg/mL dihydroxybenzoïc acid (DHB) in chloroform/methanol (1:2, v/v) were mixed with 5 µL of the sample extract in chloroform/methanol (2:1, v/v). 1-2 µL of sample was spotted on MALDI plate with a glass capillary tube. MS and MS^n spectra were acquired on an Axima Resonance (Shimadzu, Kyoto, Japan) in reflectron mode. For MS^2 experiments, ion selection was set from 250 to 500 and collision energy was tuned from 300 eV to 600 eV.

Nuclear Magnetic Resonance

Flash purified GPL were dried and dissolved in a mixture of $CDCl_3/CD_3OD$ (2:1, v/v) with 0.03 % trimethylsilane (EURISOTOP, France) three times then dissolved in a final volume of 270 µL. The sample was then introduced into a 3 mm glass tube (SHIGEMI, Allison Park, PA, US). A TBI probe was used to observe ^1H and ^{13}C nuclei at 293°K on an AVANCE II system (BRUKER BIOSPIN GmbH, Germany). Impulsion sequences used for homonuclear and heteronuclear experiments were from the manufacturer. After acquisition, phase correction and calibration on methanol signals were performed for $\delta\ ^1H$ and $\delta\ ^{13}C$.

Statistical analyses

Statistical analyses were performed on Prism 9.0 (Graphpad) and detailed for each figure legend: *$P \leq 0.05$, ** $P \leq 0.01$, and *** $P \leq 0.001$.

SUPPLEMENTAL INFORMATION

Figure S1. The unmarked deletion strategy was used to individually or simultaneously delete the three *M. abscessus* genes that encode GPL glycosyltransferases

(A) The *gtf1* gene is sandwiched between the *rmt4* and *atf1* genes; *gtf2* is wedged between *rmt3* and *fmt*; finally, *gtf3* is positioned to the right of *rmlA* and to the left of *rmlB*. Plasmids pUX1-katG-*gtf1*, pUX1-katG-*gtf2* and pUX1katG-*gtf3* were generated to remove the *Mab-gtf1*, *Mab-gtf2* and *Mab-gtf3* genes by double-homologous recombination. Genomic fragments of 1039, 1031 and 1014 bp corresponding of the left arms DNA sequences of the *Mab-gtf1*, *Mab-gtf2* and *Mab-gtf3*, respectively, were amplified by PCR and subcloned into the PacI and MfeI sites of plasmid pUX1-*katG* (Daher et al., 2020; Richard et al., 2019). The right arms DNA sequences of the *Mab-gtf1*, *Mab-gtf2* and *Mab-gtf3* were amplified from genomic DNA by PCR (1043, 1033 and 998 bp, respectively) and cloned into the MfeI and NheI sites of plasmid pUX1-*katG*. The resulting suicide plasmids (lacking motifs for episomal replication or mobile elements promoting chromosomal integration) were used to transform *M. abscessus*, in which they could only propagate *via* homologous recombination between the cloned sequences and their chromosomal homologous sequences. The first recombination events were selected in the presence of kanamycin. Single red fluorescent tdTomato-expressing clones were subjected to the second round of recombination selected on isoniazid and screened for double crossover phenotypes, i.e., loss of red fluorescence, sensitivity to kanamycin, and resistance to isoniazid. Dotted lines represent the size (indicated above each line) of the expected PCR products in *M. abscessus* WT, Δ1, Δ2, and Δ3. Black arrows represent the primers used for PCR analysis.

(B) PCR analysis demonstrating the deletion of *gtf1, gtf2, gtf3, gtf1/gtf2, gtf1/gtf3, gtf2/gtf3* and *gtf1/gtf2/gtf3* in the various mutant strains. Genomic DNA from WT bacteria was used to amplify the intact *gtf1* or *gtf2* or *gtf3* loci. Amplicons were subjected to sequencing to confirm the deletion of *gtf1* or *gtf2* or *gtf3* genes.

(C) The *gtf1, gtf2* and *gtf3* mutants were complemented using the integrative vector pMV306 containing the open reading frames of *gtf1* or *gtf2* or *gtf3* fused to a HA tag on the C-terminal side. In the complemented strains, *gtf1* expression was controlled by the *hsp60* promoter while *gtf2* and *gtf3* expression levels were dictated by their own promoters respectively. The molecular weight in kDa is indicated for each glycosyltransferase fused with an HA tag at the bottom of each schematic illustration.

(D) Western blot analysis of Δ1_C, Δ2_C, and Δ3_C strains expressing the different Gtf proteins in fusion with an HA tag (left panel). KasA was included as a loading control (right panel).

Figure S2. Mass spectrometry analysis of deacetylated polar glycolipids.

(A) MALDI-TOF-MS spectra acquired in positive mode of *Mab S* show signals patterns at *m/z* 1174/1202 for deacetylated GPL-2a and 1320/1348 for deacetylated GPL-3. Single deletion of gtf3 clearly showed a similar cluster at *m/z* 1174/1202 for deacylated GPL-2a.

(B) MALDI-TOF-MS^2 spectrum in positive mode of wild-type deacylated GPL-3 parent ion at *m/z* 1348 shows fragment Da (in bold) compared to MS^2 spectrum of native GPL-3 **(Figure 1E)**, which confirms the positions of acetyl groups on dTal.

(C) MALDI-TOF-MS^2 spectrum in positive mode of wild-type deacylated GPL-2a parent ion at *m/z* 1202 shows fragments ions with -84Da (in bold) compared to MS^2 spectrum of native GPL-2a (Figure 1D), which confirms the positions of acetyl groups on dTal.

Figure S3. Structural analysis of the GPL profile in various *gtfs* mutants.

(A) MALDI-TOF-MS spectrum in positive mode of low R_f GPL-2b isolated from Δ1 (upper panel) and MALDI-TOF-MS^2 spectrum of parent ion at *m/z* 1188 (lower panel) confirm the presence of a di-*O*-methylated di-rhamnosyl motif and the absence of dTal.

(B) MALDI-TOF-MS spectrum in positive mode of high R_f GPL-1b isolated from Δ1 (upper panel) and MALDI-TOF-MS^2 spectrum of parent ion at *m/z* 1042 (lower panel) confirm the presence of a single di-*O*-methyl Rha and the absence of dTal.

(C) MALDI-TOF-MS spectrum in positive mode of high R_f GPL-1b isolated from Δ1,3 (upper panel) and MALDI-TOF-MS^2 spectrum of parent ion at *m/z* 1042 (lower panel) confirm the presence of a single di-*O*-methyl Rha and the absence of dTal.

(D) ^{1}H-^{13}C HSQC spectrum of high R_f GPL-1b from Δ1,3 confirmed the presence of a single di-*O*-methyl Rha substituted in C3 and C4 positions. Another *O*-methyl group observed at ^{1}H-^{13}C 3.28/56.8 ppm was attributed to 3-methoxy lipid as previously described (Daher et al., 2020). Alpha-carbons from each amino-acid were also detected and correlated with respective beta carbons by ^{1}H-^{1}H COSY spectrum (data not shown). Two amino-alcohol alaninol and valinol are also observed, which confirmed the presence of the two variants GPL.

(E) TLC analysis of GPL fractions developed in $CHCl_3/CH_3OH/H_2O$ (90/10/1) and stained with phosphomolybdic acid revealed two intense bands corresponding to accumulated lipopeptide for mutant Δ1,2. Lower intensity was observed for mutant Δ*2*. The circled band was further analyzed by MALDI-MS and NMR.

(F) MALDI-TOF MS spectrum in positive mode of the lipopeptide isolated from Δ1,2 (**Figure S3E** circled lower Rf band) showed two ions at *m/z* 838 and 866. This mass shifted at *m/z* 866 and 894 for the higher R_f accumulating band.

(G) ^{1}H-^{1}H COSY spectrum allows the amino-acid sequencing of the lipopeptide isolated from Δ1,2 (**Figure S3E**, circled lower Rf band). Higher Rf lipopeptide did not show the presence of alaninol residue (data not shown).

Figure S4. Deletion of *gtf1* or *gtf2* promotes bacterial sedimentation in *in vitro* culture, abolishes the ability of bacilli to form thick and filamentous biofilms on a liquid surface and increases the susceptibility of *Mab* to rifabutin.

(A) The 3 glycosyltransferases are not involved in the growth of bacilli *in vitro*. Growth curve of parental S, wild-type R, Δ1, Δ1_C, Δ2, Δ2_C, Δ3, Δ3_C, Gtf3_ov, Δ1,2, Δ1,3, Δ2,3 and Δ1,2,3 strains in 7H9 medium at 37 °C. Data is representative of three independent experiments.

(B) Bacilli that do not express Gtf1 or Gtf2 sediment rapidly in *in vitro* culture. Like the parental S strain, but unlike the R variant, Δ3 does not sediment rapidly in liquid culture. However, the Δ1, Δ2, double and triple mutant strains do sediment rapidly in *in vitro* culture. Note that the Gtf3-ov strain partially sedimented for the same amount of time. Finally, the Δ2_C variant sedimented like an R strain but forming a hill at the bottom of the glass tube. Experiments were carried out three times.

(C) Strains belonging to the S morphotype form filamentous biofilms on the surface of the liquid M63 medium while R variants establish a thin layer dotted with spaced white spots. Pellicle-forming capabilities of *M. abscessus* S, R, Δ1, Δ1_C, Δ2, Δ2_C, Δ3, Δ3_C, Gtf3_ov, Δ1,2, Δ1,3, Δ2,3 and Δ1,2,3 strains. Experiments were carried out three times.

(D) Biofilm formation (liquid/air interface) and planktonic growth (solid/liquid interface) in glass tubes. The *M. abscessus* S, R, Δ1, Δ1_C, Δ2, Δ2_C, Δ3, Δ3_C, Gtf3_ov, Δ1,2, Δ1,3, Δ2,3 and Δ1,2,3 strains were grown, in static conditions at 37 °C, in M63 medium and in glass tubes. Pictures were taken after 6 days of incubation.

(E) Absence of gtf1 or gtf2 makes bacilli 4 times more susceptible to rifabutin. Drug susceptibility profile of *M. abscessus* S, R, Δ1, Δ1_C, Δ2, Δ2_C, Δ3, Δ3_C, Gtf3_ov, Δ1,2, Δ1,3, Δ2,3 and Δ1,2,3 strains to various antibiotics (cefoxitin, imipenem, bedaquiline, amikacin and rifabutin) in CaMBH. MIC (µg/mL) were determined following the CLSI guidelines.

Figure S5. Inactivation of the *gtf1* or *gtf2* genes in the smooth morphotype variant gives the bacilli the ability to establish cords *in cellulo.*

One immunofluorescent field per strain was taken at 3 days post-infection showing macrophages infected with *M. abscessus* expressing Tdtomato (red). The surface of the macrophages was detected using anti-CD43 antibodies (green). The nuclei were stained with DAPI (blue). The S, Δ1_C, Δ3 and Δ3_C strains belong to the smooth morphotype and therefore do not form cords *in cellulo*. In contrast to the smooth variants, the rough strains which are R, Δ1, Δ2, Δ2_C as well as the double and triple mutants form intracellular and extracellular cords *ex vivo*. C.: cord. The scale bars for all images taken in normal confocal mode represent 20 µm.

Two images for each of the R, Δ1 and Δ2 strains were taken in Z-stack Airyscan mode to illustrate in 3D the cords established inside the macrophages as well as outside the cells. A Z-stack series was collected with a Zeiss LSM880 Airyscan confocal microscope and images were assembled and reconstructed with Imaris 3D

software. I.C.: intracellular cord, E.C.: extracellular cord. The scale bars for the three 3D images showing either the intracellular cords or the other three extracellular cords represent 3 µm and 5 µm, respectively.

Figure S6. Uptake inhibition was not observed when pre-treated macrophages were infected with the strains: S or Δ1 or Δ2 or Δ3 or Δ1,3. Invasion of the strains (S or Δ1 or Δ2 or Δ3 or Δ1,3) was not reduced in macrophages pretreated with mannan, laminarin and methyl-α-D-glucopyranoside. CFU were determined at 3 hpi. Data are mean values ± SD for four independent experiments (each time in triplicate) (n=12).

Figure S7. Steric hindrance of MR and CR3 receptors reduces the average number of internalized GPL-3-coupled beads per macrophage

(A) Maximum intensity projection reconstruction of two three-dimensional macrophages (red) containing fluorescent beads coupled to GPL-3 (green). The two images were created by merging serial scans of extremely thin (0.18 µm) cell sections, observed under confocal microscopy (LSM880) in Airyscan Z-stack mode at 63x magnification. Showing in the y/z plane the depth of the two macrophages. The nuclei were stained with DAPI (blue).

(B) On average, macrophages pre-treated with mannan or laminarin or methyl-α-D-glucopyranoside ingested less GPL-3-coupled beads than those not pre-treated. Quantification of the average number of beads alone or coupled to GPL-1b, GPL-2a, GPL-2b or GPL-3 per macrophage was performed after 4 hours of phagocytosis. The red bar in each violin plot represents median. The colored area of a violin plot corresponds to the probability density of the data and contains first and third quartiles. Data are mean values ± SD for three independent experiments (each time in triplicate) (n=900 macrophages containing beads per condition). One-tailed Mann−Whitney test: ***$p < 0.001$.

(C) Representative fluorescent images showing the impact of neutralizing anti-CR3 and anti-Dectin1 antibodies on the internalization of GPL-2a- or GPL-3-coupled beads by macrophages. CD43 (red), DAPI (blue), fluorescent beads (green). White arrows indicate the presence of fluorescent beads inside macrophages. Scale bars represent 20 µm.

Movies 1 and 2. These two movies show two different macrophages that phagocytosed 3 or 8 green fluorescent beads coupled to GPL3. Image acquisition was performed using a confocal microscope in AiryScan Z-stack mode. Both videos were generated using the Zen program (blue edition).

Table S1. Primers used in this study. Restriction sites are in bold and underlined.

Number	5'→3' sequence	Restriction site	F (sense), R (antisense)
Cloning in pUX1-*katG*			
1	gaga**TTAATTAA**GAAATATCTGGCGACA TCGGTTCATAAGATTTTTTGAC	PacI	To clone the left arm of *gt* in pUX1-*katG* (F)
2	gaga**CAATTG**GTAACTCGCCAGCACAAATTTCATCGCTTC	MfeI	To clone the left arm of *gt* in pUX1-*katG* (R)
3	gaga**CAATTG**GAAAGTGCTGTCGCTGCCGCG	MfeI	To clone the right arm of *gtf1* in pUX1-*katG* (F)
4	gaga**GCTAGC**GCAATGACAAAGAACAGCAACAGATTCAGACTG	NheI	To clone the right arm of *gtf1* in pUX1-*katG* (R)
5	gaga**TTAATTAA**CTTGACAAAGCGGTACATCCGGTATTCG	PacI	To clone the left arm of *gt* in pUX1-*katG* (F)
6	gaga**CAATTG**CACGCTGACGGATGGTTCGACATC	MfeI	To clone the left arm of *gt* in pUX1-*katG* (R)
7	gaga**CAATTG**GCAGTCTCCGCTCAGATGACCTC	MfeI	To clone the right arm of *gtf2* in pUX1-*katG* (F)
8	gaga**GCTAGC**GATTCCTCTTGATCGCGATGCTGCG	NheI	To clone the right arm of *gtf2* in pUX1-*katG* (R)
9	gaga**TTAATTAA**TTGTCGTAGAAGTACAGCCCCGGTA	PacI	To clone the left arm of *gt* in pUX1-*katG* (F)
10	gaga**CAATTG**TTTCATGACGGTATAGACCTCCCCGAT	MfeI	To clone the left arm of *gt* in pUX1-*katG* (R)
11	gaga**CAATTG**TCTCTGGTCTCGGACCTACGCA	MfeI	To clone the right arm of *gtf3* in pUX1-*katG* (F)
12	gaga**GCTAGC**TTGTTTCTCACGTGCCAACCGCG	NheI	To clone the right arm of *gtf3* in pUX1-*katG* (R)
Primers to verify double homologous recombination			
13	GTGTTCGACTCGGTGGTCGTGATTCAC	-	To check double homologous recombinatio Δ1 (F)
14	GTTTTTCCACGACAAACCAACTGAAAGCC	-	To check double homologous recombinatio Δ1 (R)
15	TCGACGACGTTCATCACTCAACTATACCTATC	-	To check double homologous recombinatio Δ2 (F)
16	CTTTCAGTTGGTTTGTCGTGGAAAAACGCG	-	To check double homologous recombinatio Δ2 (R)
17	GAATCGAACGTTCCGGTGTCCAG	-	To check double homologous recombinatio Δ3 (F)
18	CATCGCGAAACTTCCCGACAACG	-	To check double homologous recombinatio Δ3 (R)
Cloning in pMV306-KanR			
19	gaga**CAATTG**CCATGAAATTTGTGCTGGCGAGTTACGGAACG	MfeI	To clone the *gtf1-HA* ORF pMV306 (F)
20	gaga**GTCGAC**CTAAGCGTAATCTGGAACATCGT ATGGGTATGCCGAACACCTCGCCTGCG	SalI	To clone the *gtf1-HA* ORF pMV306 (R)
21	gaga**TCTAGA**TGGACGACTCCGTACCATCGACGAA	XbaI	To clone the *gtf2-HA* ORF pMV306 (F)

22	gaga**GTCGAC**CTAAGCGTAATCTGGAACATCGTAT GGGTACACCGCTTTTCGGCCGGCGGT	SalI	To clone the *gtf2-HA* ORF pMV306 (R)
23	gagaga**GGTACC**ACCAGCGGTTTGTCGTAGACCG	KpnI	To clone the *gtf3-HA* ORF pMV306 (F)
24	gagaga**GAATTC**CTAAGCGTAATCTGGAACATCGTA TGGGTATGGGTGGGAAGCCTTTGCCTC	EcoRI	To clone the *gtf3-HA* ORF pMV306 (R)
Cloning in pMV261-KanR			
25	gagaga**TGGCCA**CCATGGCCGAGAATATTGACGTCCATTCTG	MscI	To clone the *gtf3-HA* ORF pMV261 (F)
26	gagaga**GAATTC**CTAAGCGTAATCTGGAACATCGT ATGGGTATGGGTGGGAAGCCTTTGCCTC	EcoRI	To clone the *gtf3-HA* ORF pMV261 (R)

Figure 1

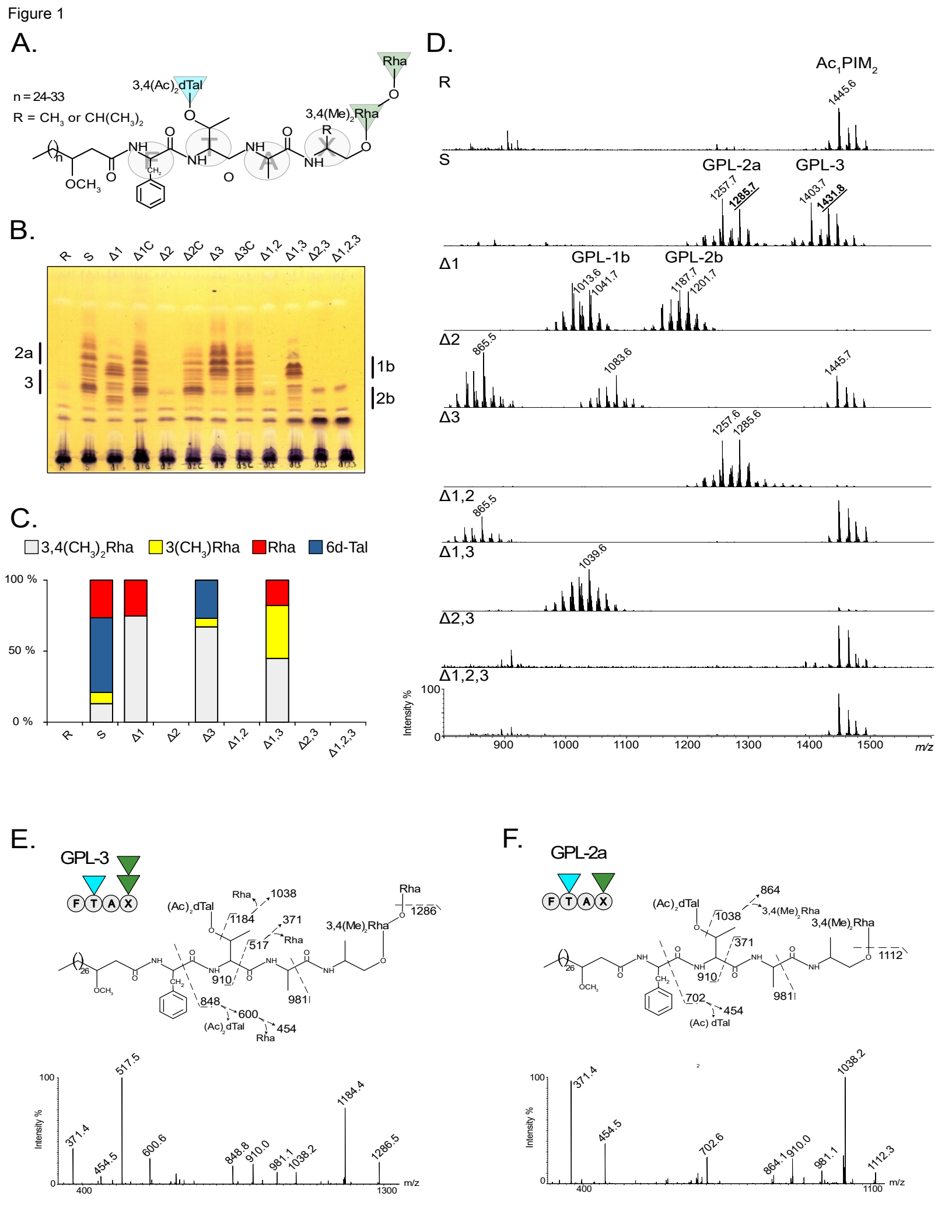
A.
n = 24-33
R = CH3 or CH(CH3)2
3,4(Ac)2dTal
3,4(Me)2Rha
Rha
OCH3
B.
R S Δ1 Δ1C Δ2 Δ2C Δ3 Δ3C Δ1,2 Δ1,3 Δ2,3 Δ1,2,3
2a
3
1b
2b
C.
3,4(CH3)2Rha
3(CH3)Rha
Rha
6d-Tal
100 %
50 %
0 %
D.
Ac1PIM2
R
1445.6
S
GPL-2a
GPL-3
1257.7
1285.7
1403.7
1431.8
Δ1
GPL-1b
GPL-2b
1013.6
1041.7
1187.7
1201.7
Δ2
865.5
1083.6
1445.7
Δ3
1257.6
1285.6
Δ1,2
865.5
Δ1,3
1039.6
Δ2,3
Δ1,2,3
Intensity %
m/z
E.
GPL-3
Rha
1038
(Ac)2dTal
1184
371
517
Rha
3,4(Me)2Rha
1286
910
981
848
600
454
(Ac)2dTal
Rha
517.5
1184.4
371.4
454.5
600.6
848.8
910.0
981.1
1038.2
1286.5
F.
GPL-2a
864
(Ac)2dTal
1038
3,4(Me)2Rha
3,4(Me)2Rha
371
1112
910
981
702
454
(Ac) dTal
1038.2
371.4
454.5
702.6
864.1
910.0
981.1
1112.3

Figure 2

A.

GPLs glycoforms	Peptido Lipid FTAX	GPL-1a FTAX	GPL-1b FTAX	GPL-2a FTAX	GPL-2b FTAX	GPL3 FTAX
(detected *m/z*)	*(866)*		*(1014/1042)*	*(1258/1286)*	*(1160/1188)*	*(1404/1432)*
(saponified)	(-)		(-)	(+)	(-)	(+)
R						
S				X		X
Δ1			X		X	
Δ2	X					
Δ3				X		
Δ1,2	X					
Δ1,3			X			
Δ2,3						
Δ1,2,3						

B.

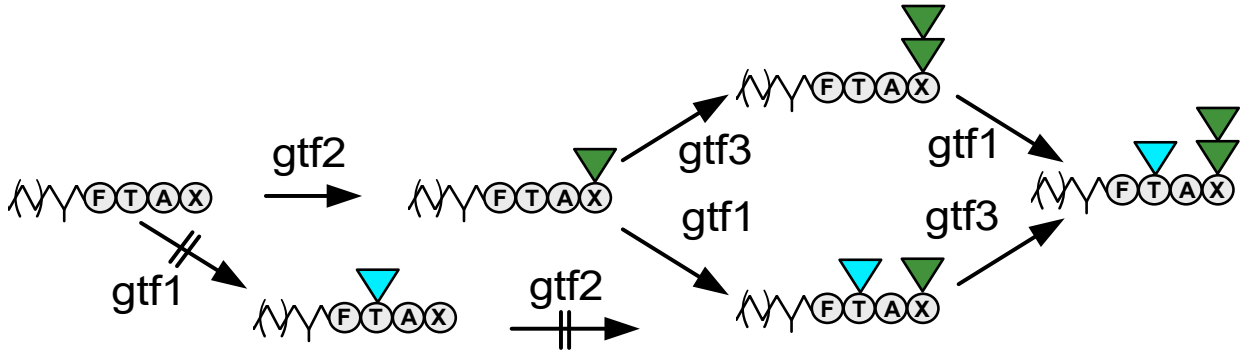

Figure 3

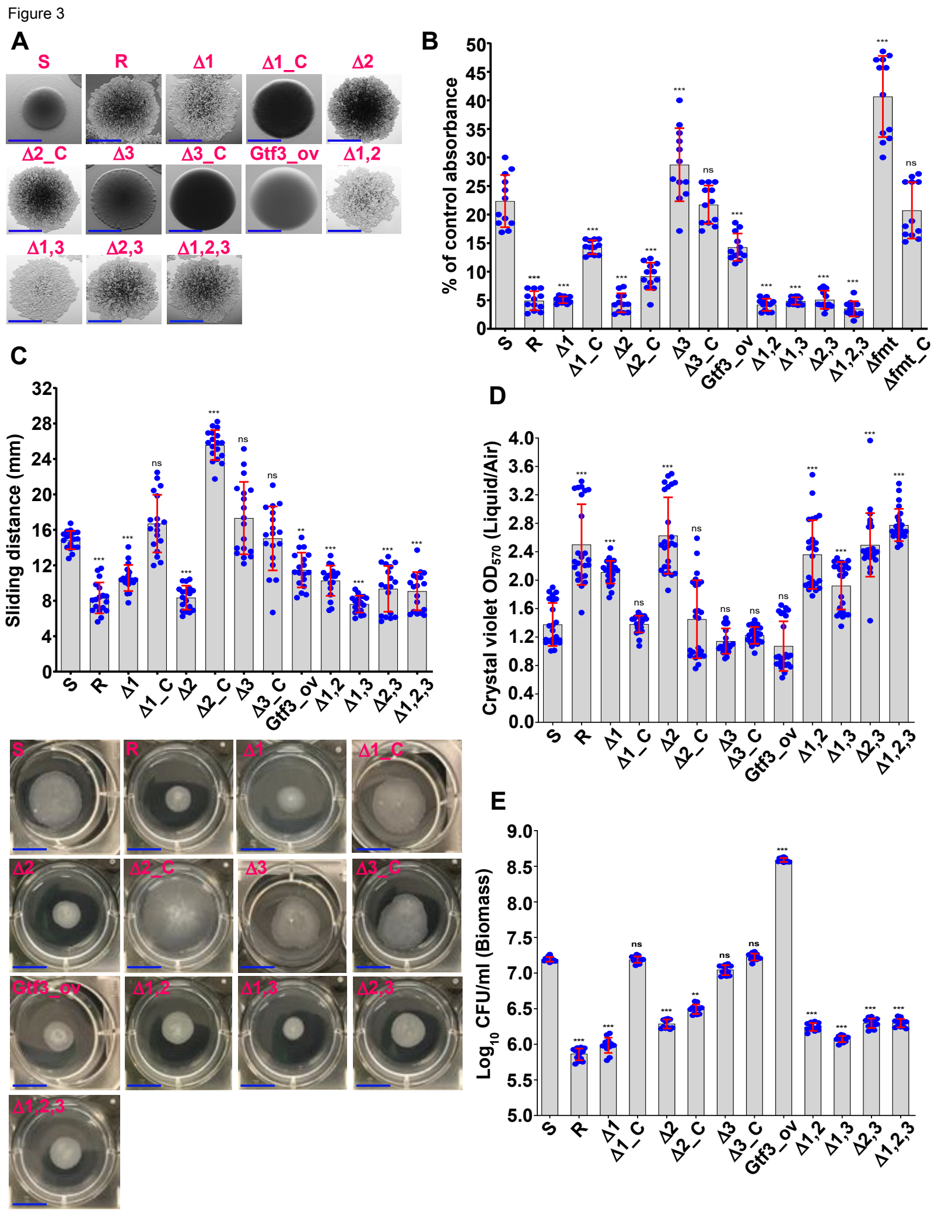
A
S
R
Δ1
Δ1_C
Δ2
Δ2_C
Δ3
Δ3_C
Gtf3_ov
Δ1,2
Δ1,3
Δ2,3
Δ1,2,3
B
% of control absorbance
Δfmt
Δfmt_C
C
Sliding distance (mm)
D
Crystal violet OD570 (Liquid/Air)
E
Log10 CFU/ml (Biomass)
ns

Figure 4

Click here to access/download;Figure;Figure 4.tif

gtf fish figure_230521.pdf

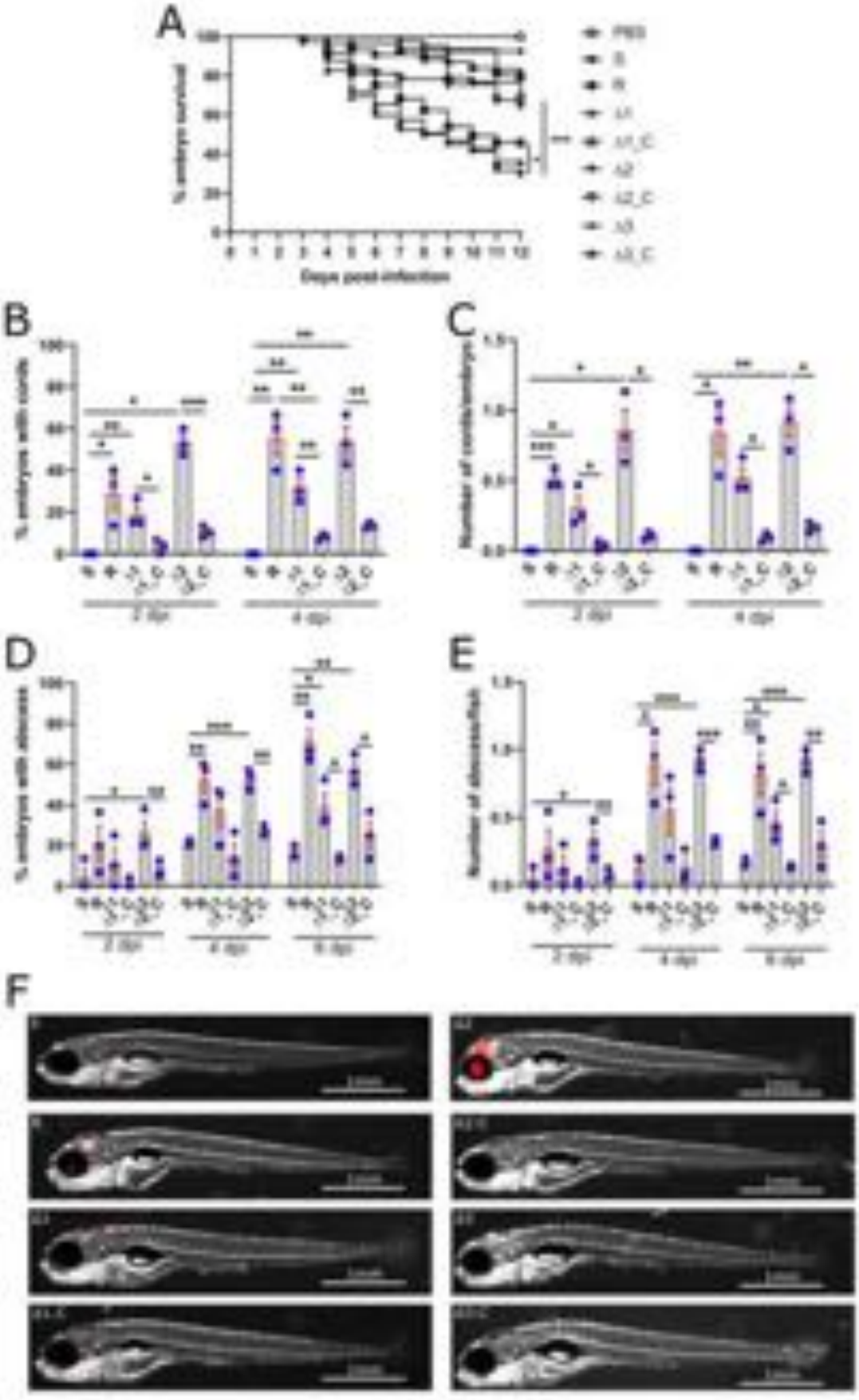

Figure 5

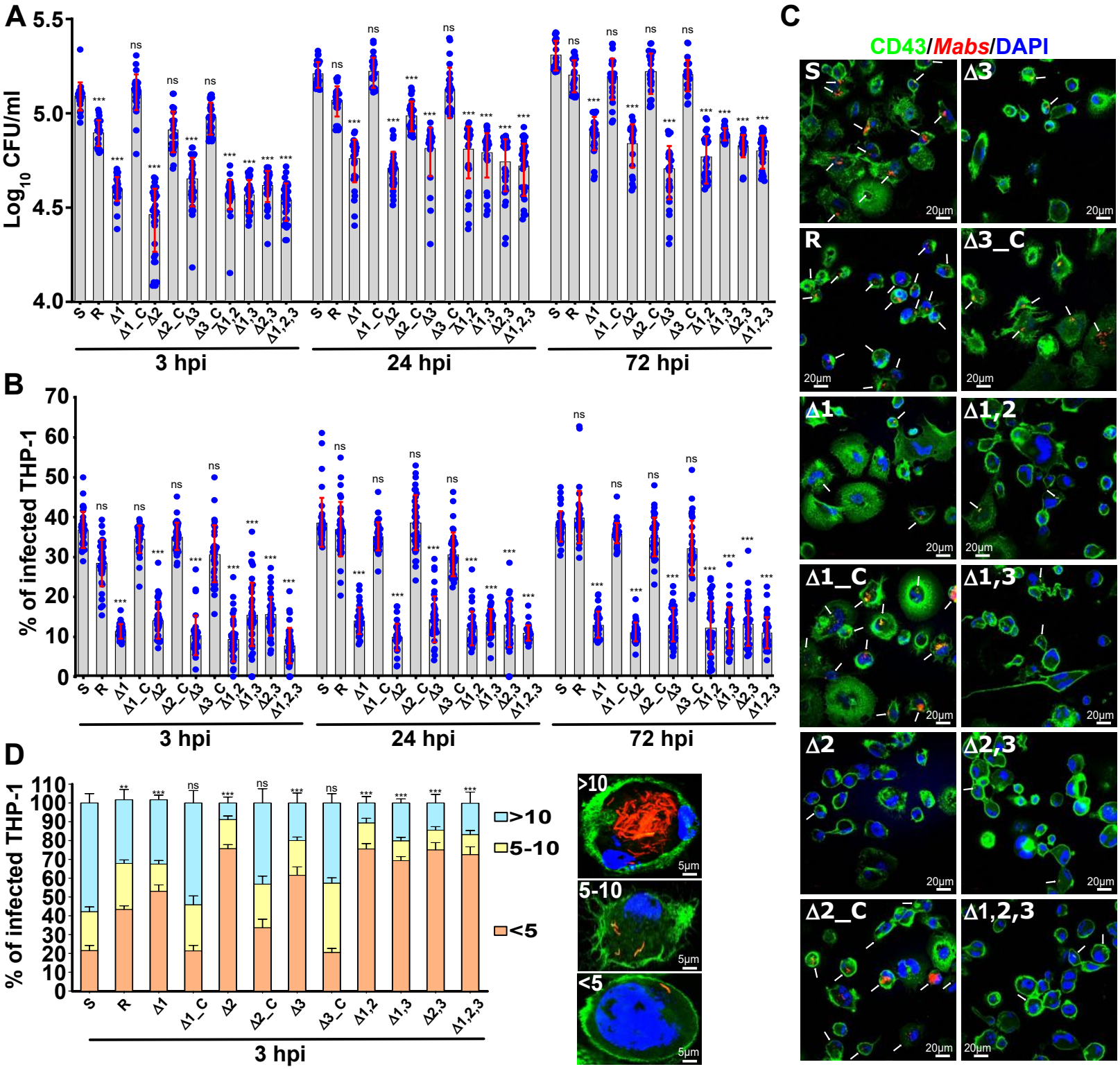
A
Log10 CFU/ml
3 hpi
24 hpi
72 hpi
B
% of infected THP-1
3 hpi
24 hpi
72 hpi
C
CD43/Mabs/DAPI
S
Δ3
R
Δ3_C
Δ1
Δ1,2
Δ1_C
Δ1,3
Δ2
Δ2,3
Δ2_C
Δ1,2,3
20μm
D
% of infected THP-1
3 hpi
>10
5-10
<5
5μm

Figure 6

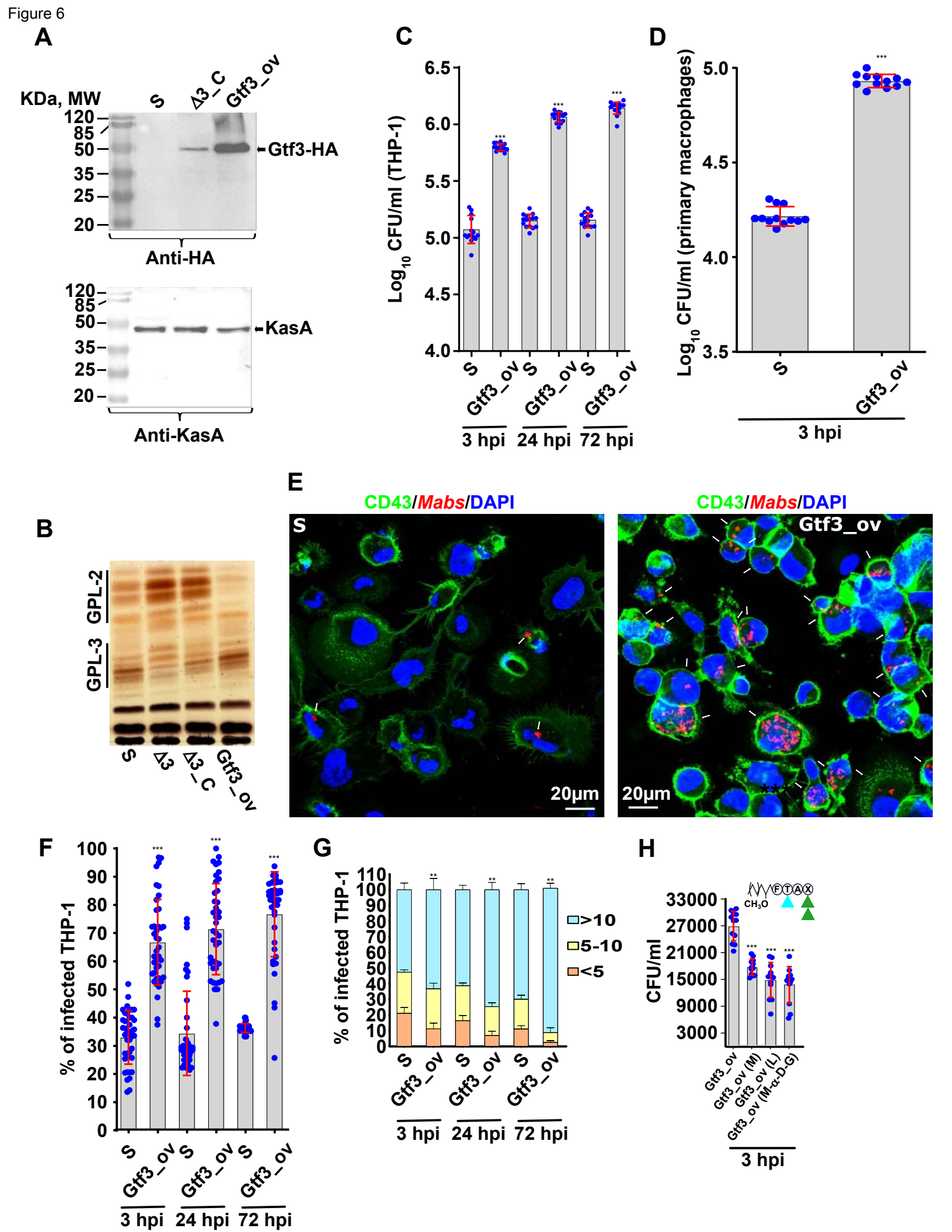
A
KDa, MW
S
Δ3_C
Gtf3_ov
120
85
50
35
25
20
Gtf3-HA
Anti-HA
KasA
Anti-KasA
B
GPL-2
GPL-3
S
Δ3
Δ3_C
Gtf3_ov
C
Log10 CFU/ml (THP-1)
3 hpi
24 hpi
72 hpi
D
Log10 CFU/ml (primary macrophages)
3 hpi
E
CD43/Mabs/DAPI
20μm
F
% of infected THP-1
G
>10
5-10
<5
H
CFU/ml
Gtf3_ov
Gtf3_ov (M)
Gtf3_ov (L)
Gtf3_ov (M-α-D-Gl)

Figure 7

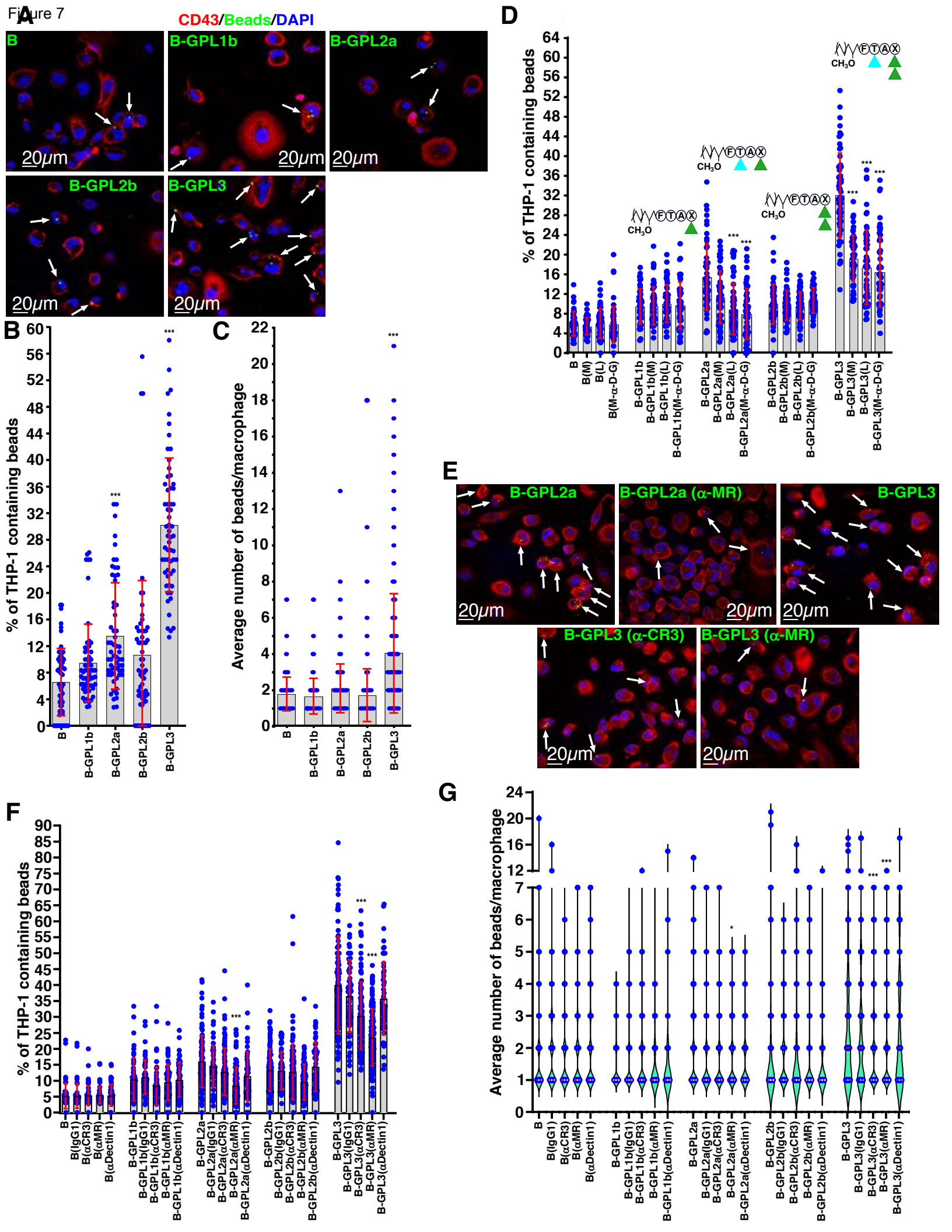
A
CD43/Beads/DAPI
B
B-GPL1b
B-GPL2a
B-GPL2b
B-GPL3
20μm
B
% of THP-1 containing beads
B-GPL1b
B-GPL2a
B-GPL2b
B-GPL3
C
Average number of beads/macrophage
D
% of THP-1 containing beads
B
B(M)
B(L)
B(M-α-D-G)
B-GPL1b
B-GPL1b(M)
B-GPL1b(L)
B-GPL1b(M-α-D-G)
B-GPL2a
B-GPL2a(M)
B-GPL2a(L)
B-GPL2a(M-α-D-G)
B-GPL2b
B-GPL2b(M)
B-GPL2b(L)
B-GPL2b(M-α-D-G)
B-GPL3
B-GPL3(M)
B-GPL3(L)
B-GPL3(M-α-D-G)
E
B-GPL2a
B-GPL2a (α-MR)
B-GPL3
B-GPL3 (α-CR3)
B-GPL3 (α-MR)
F
% of THP-1 containing beads
G
Average number of beads/macrophage

Supplemental Figure 1

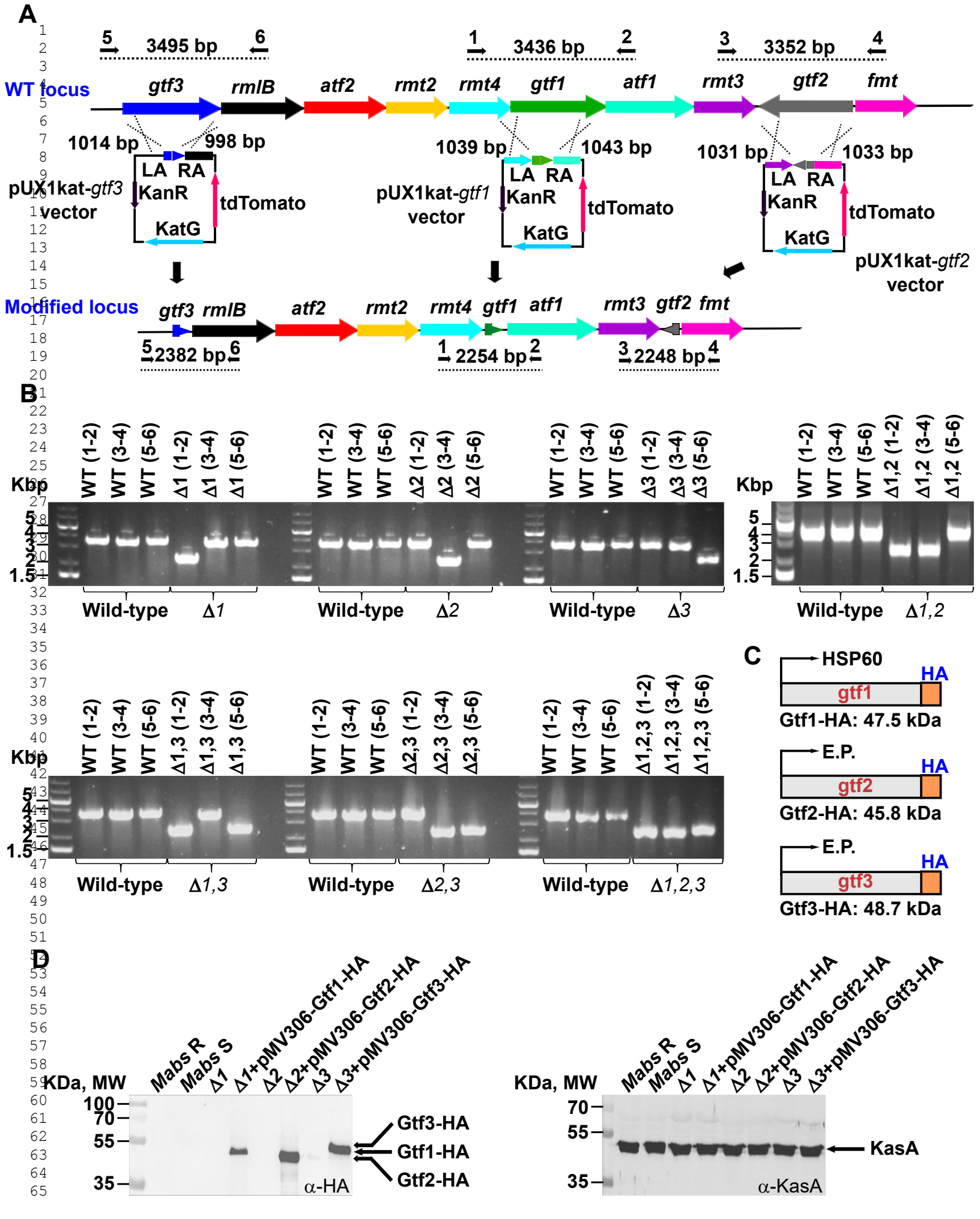

Supplemental Figure 2

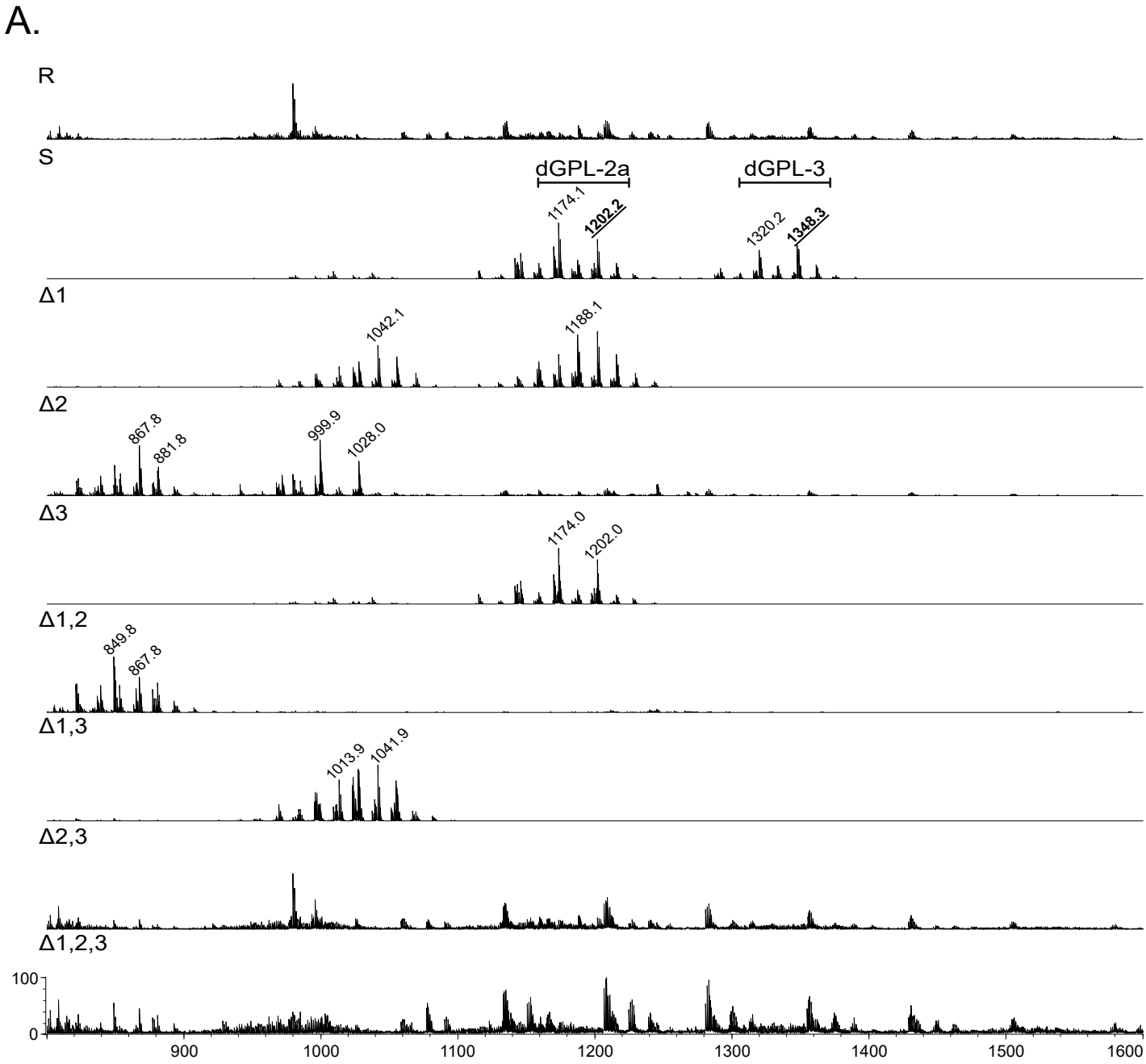

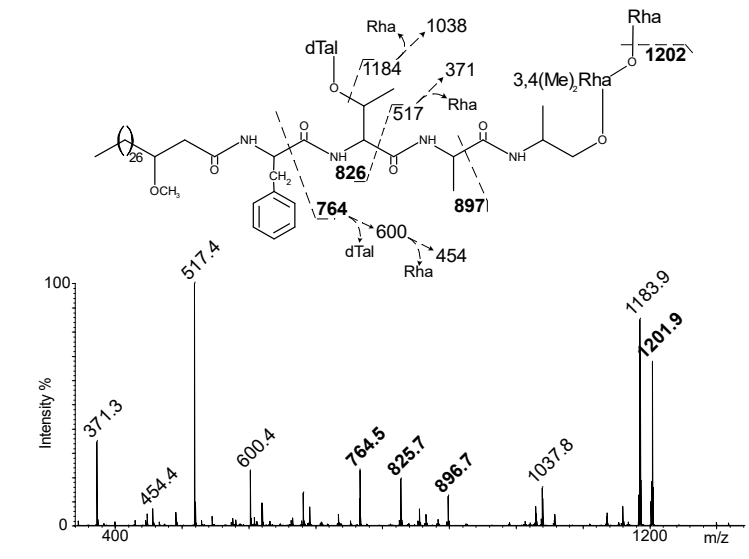

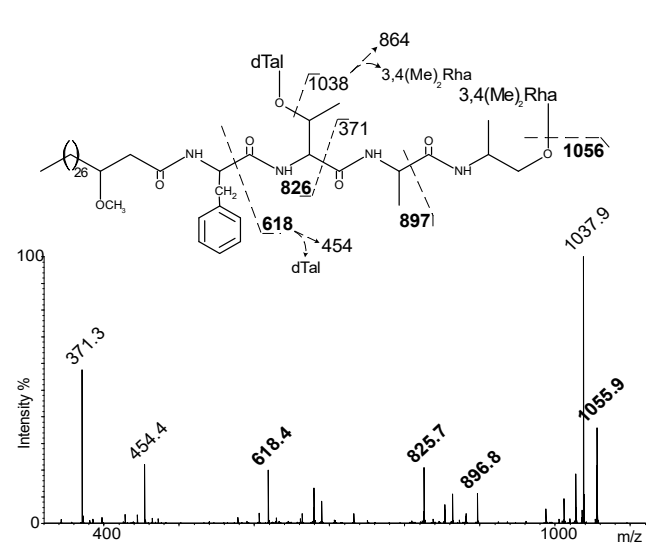

Supplemental Figure 3

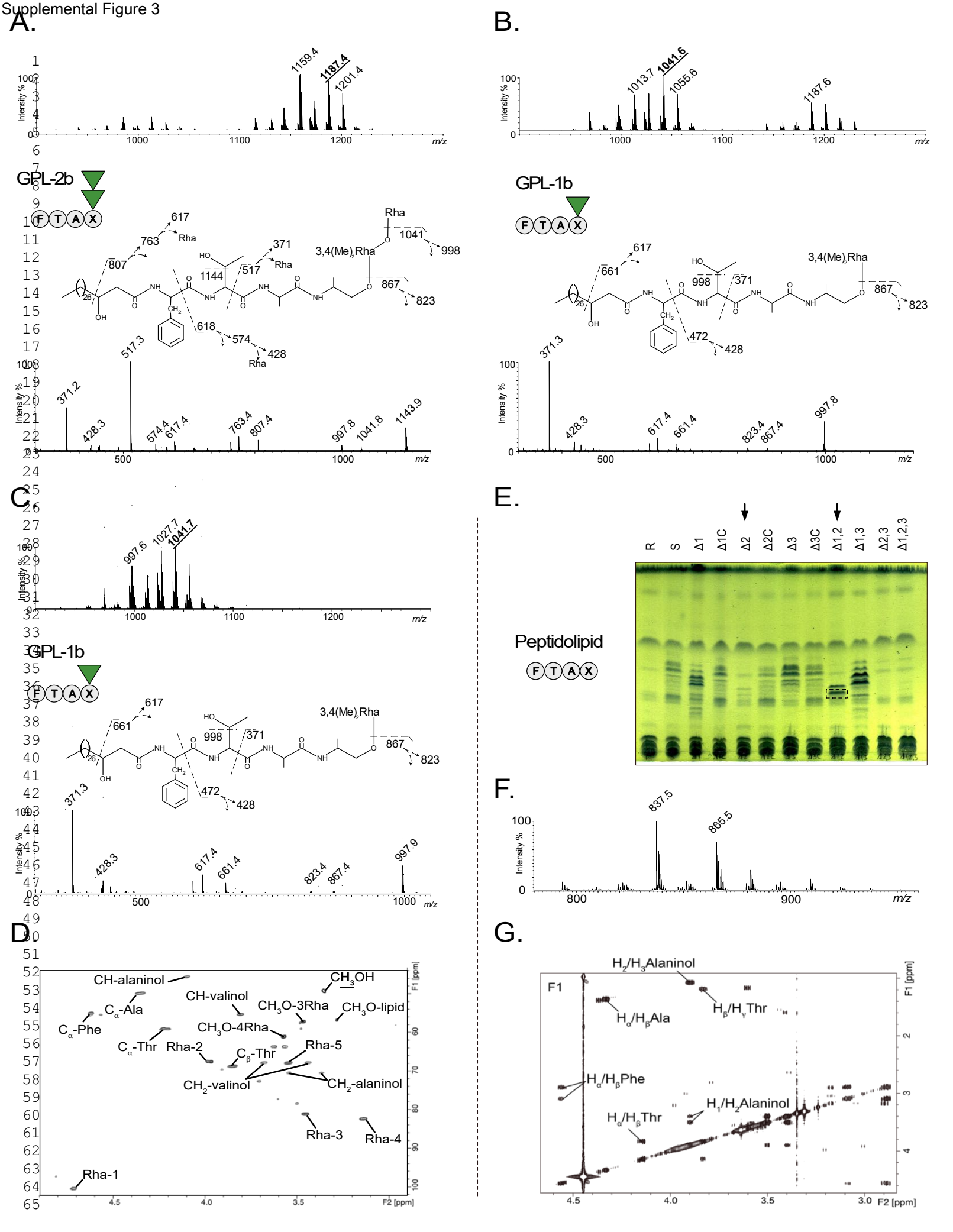

Supplemental Figure 4

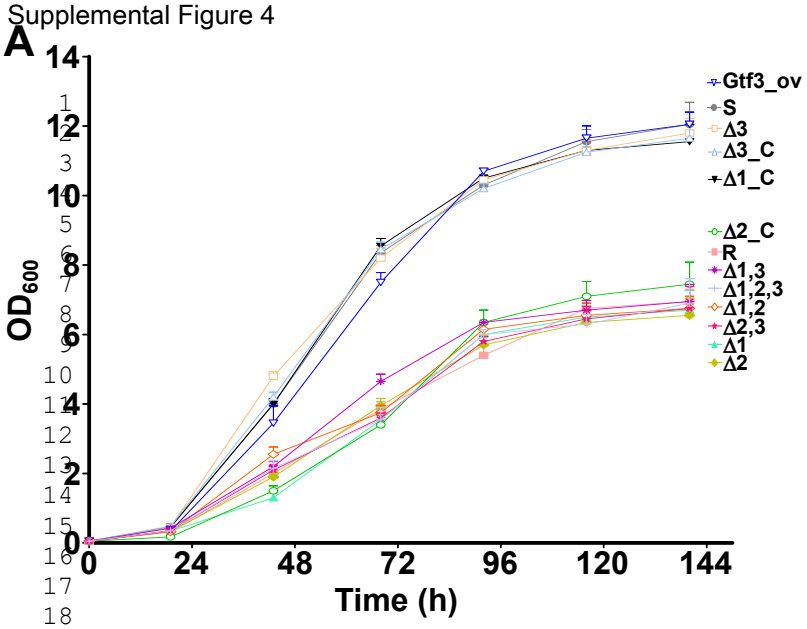

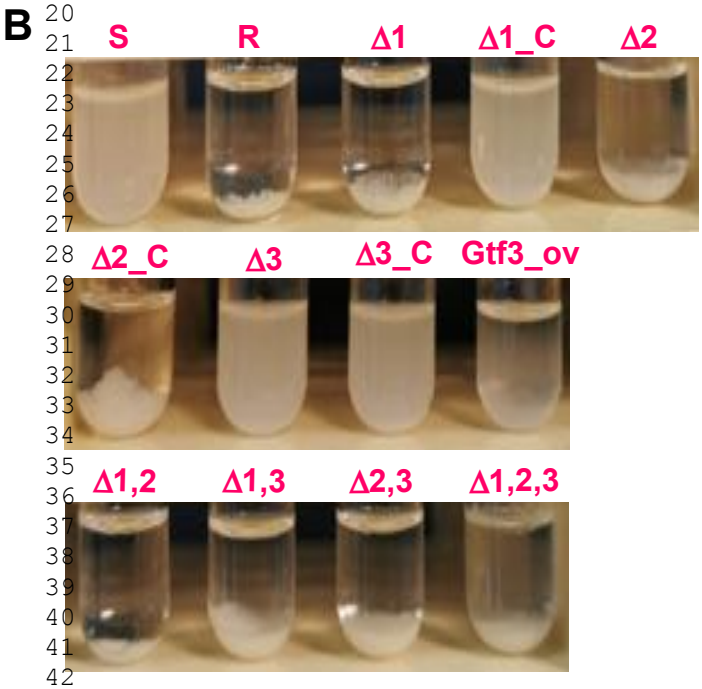

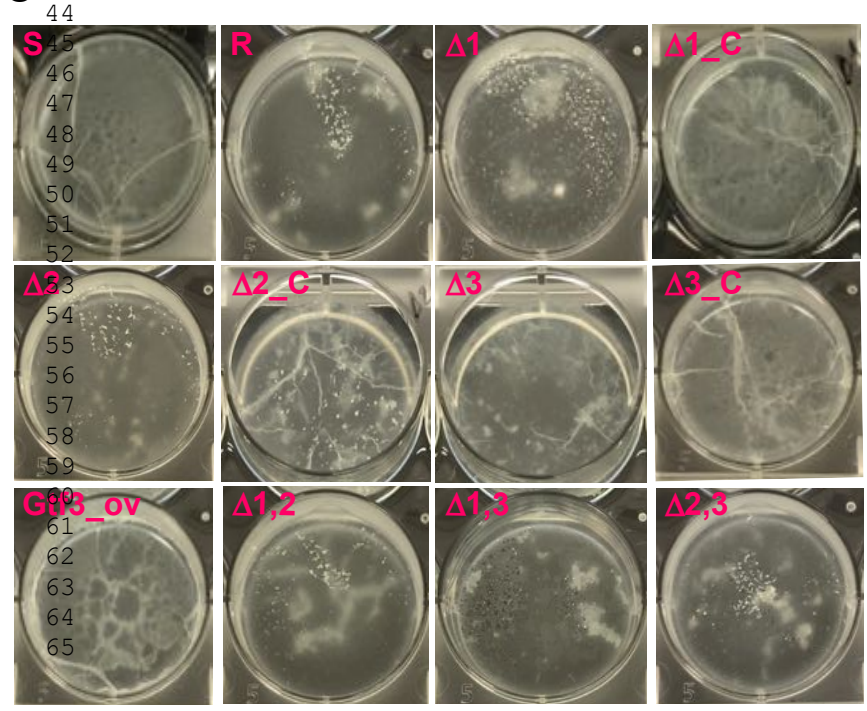

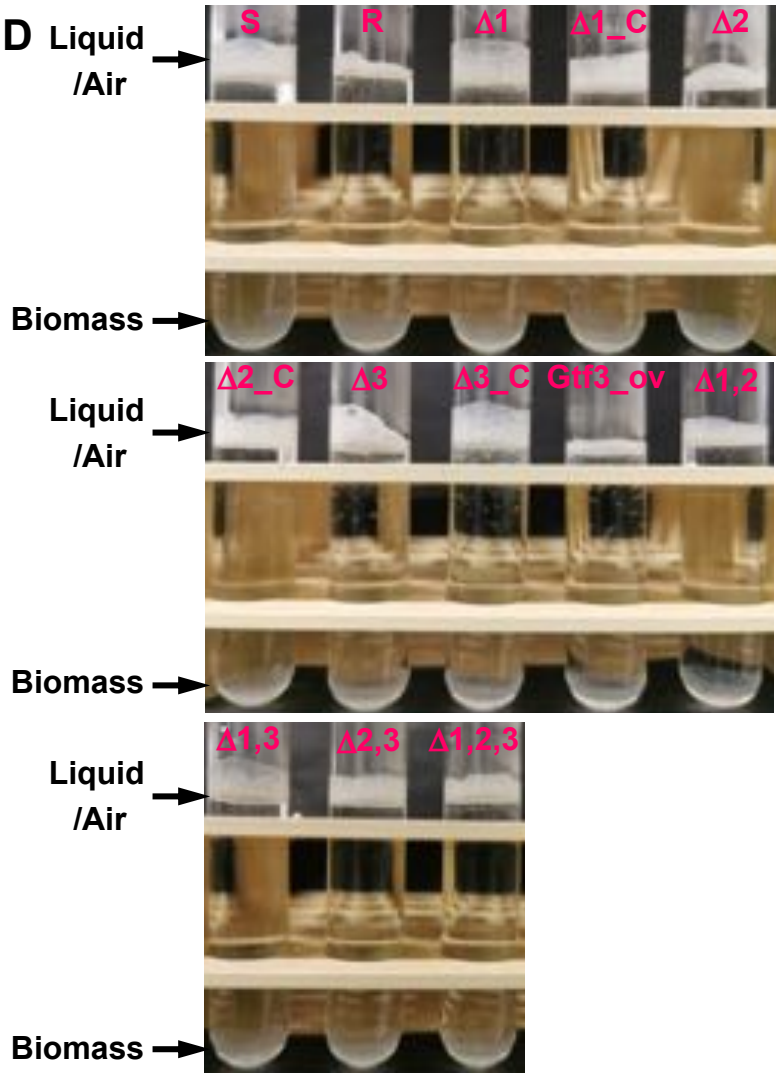

E

	CMI µg/ml				
	Cefoxitin	Imipenem	Bedaquiline	Amikacin	Rifabutin
S	64	16	0.06	32	50
R	64	32	0.06	16	12.5
Δ1	64	32	0.06	32	12.5
Δ1_C	64	16	0.06	32	50
Δ2	64	32	0.06	32	12.5
Δ2_C	64	32	0.03	32	50
Δ3	64	16	0.06	32	50
Δ3_C	64	16	0.06	32	50
Gtf3_ov	64	16	0.06	32	50
Δ1,2	64	32	0.03	32	12.5
Δ1,3	64	32	0.03	16	12.5
Δ2,3	64	32	0.06	16	12.5
Δ1,2,3	64	32	0.03	16	12.5

Supplemental Figure 5

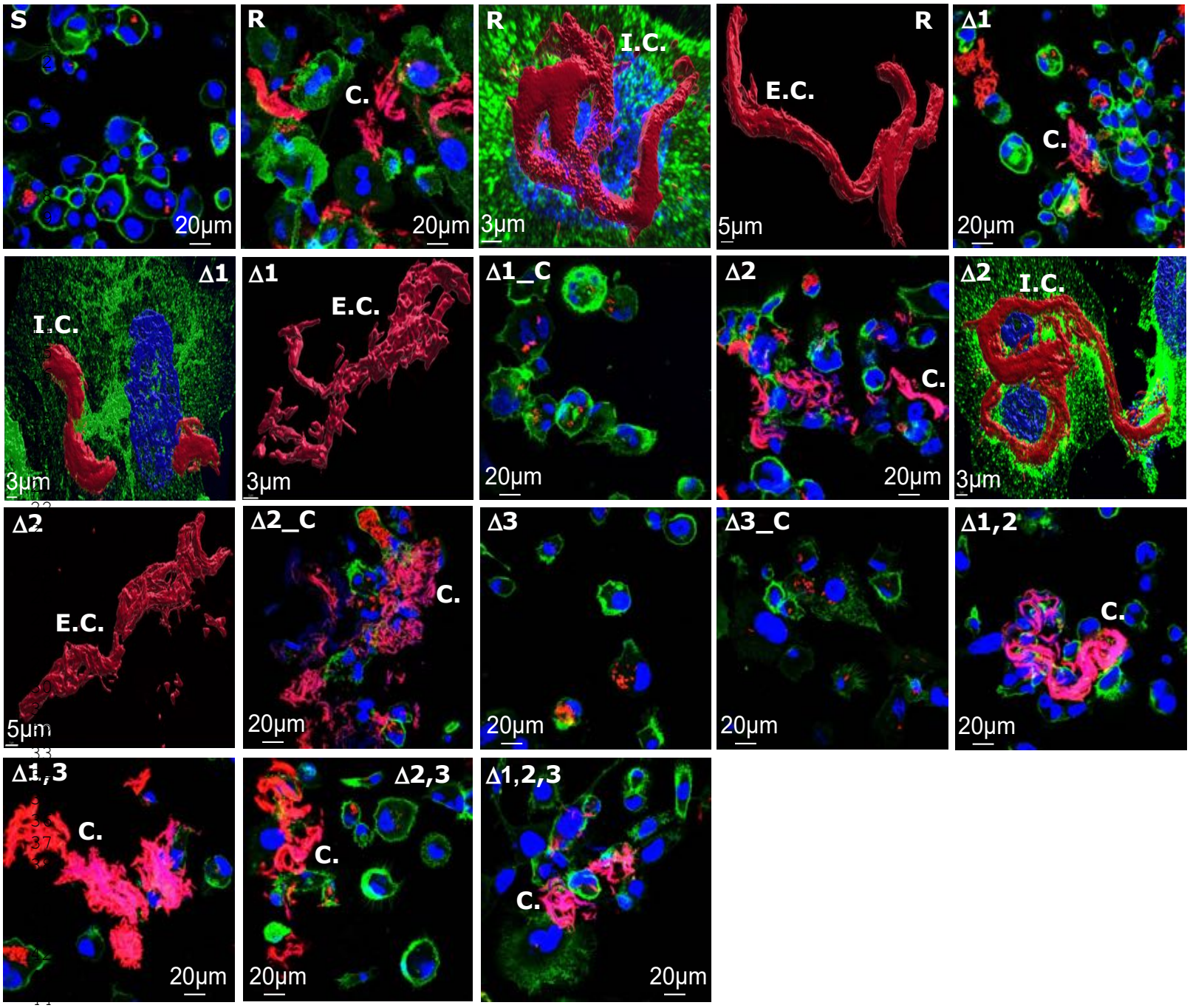

Supplemental Figure 6

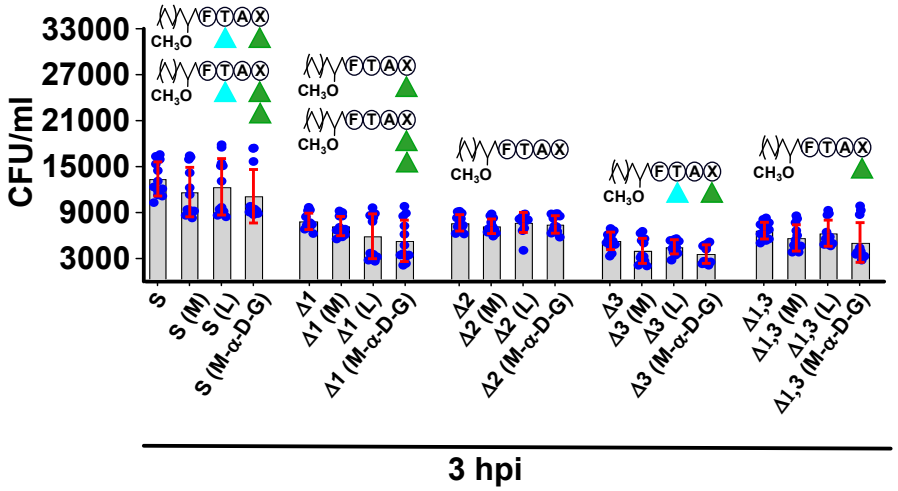

Supplemental Figure 7

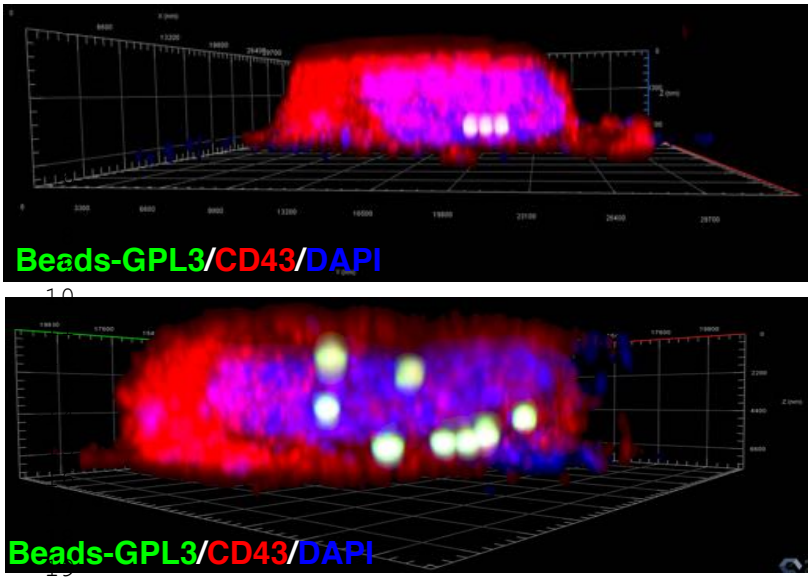

Video 1

Click here to access/download

Supplemental Videos and Spreadsheets

Movie1.avi

Video 2

Click here to access/download

Supplemental Videos and Spreadsheets

Movie2.avi